Article

Developmental Cell

The cell cycle controls spindle architecture in *Arabidopsis* by activating the augmin pathway

Graphical abstract

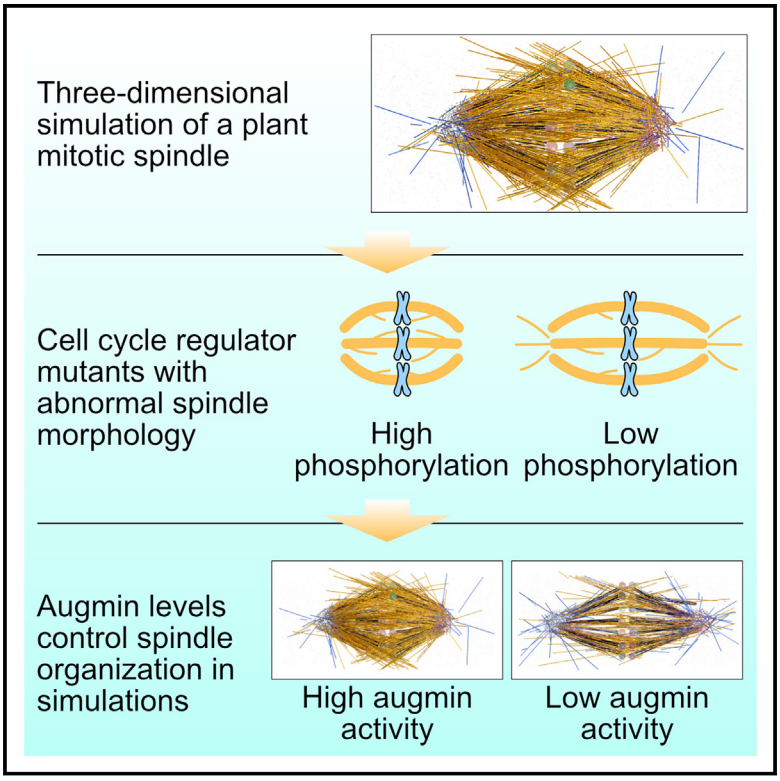

Authors

Mariana Romeiro Motta, François Nédélec, Helen Saville, ..., Geert De Jaeger, David Bouchez, Arp Schnittger

Correspondence

francois.nedelec@slcu.cam.ac.uk (F.N.), arp.schnittger@uni-hamburg.de (A.S.)

In brief

Romeiro Motta et al. show that spindle morphology is controlled by the phosphorylation of augmin performed by a cell-cycle regulator complex in *Arabidopsis*. By constructing a tridimensional simulation of the *Arabidopsis* mitotic spindle, combined with several experimental approaches, they show that changes in augmin activity largely impact spindle organization.

Highlights

- Generation of a 3D simulation of the *Arabidopsis* spindle
- B1-type CDKs together with a B3-type cyclin control spindle morphology via augmin
- The requirement of augmin for spindle morphology is recapitulated by 3D simulations

Romeiro Motta et al., 2024, Developmental Cell *59*, 1–15
November 18, 2024
https://doi.org/10.1016/j.devcel.2024.08.001

CellPress

Developmental Cell

CellPress
OPEN ACCESS

Article

The cell cycle controls spindle architecture in *Arabidopsis* by activating the augmin pathway

Mariana Romeiro Motta,[1,2,9] François Nédélec,[3,*] Helen Saville,[3] Elke Woelken,[4] Claire Jacquerie,[3] Martine Pastuglia,[5] Sara Christina Stolze,[6] Eveline Van De Slijke,[7,8] Lev Böttger,[1] Katia Belcram,[5] Hirofumi Nakagami,[6] Geert De Jaeger,[7,8] David Bouchez,[5] and Arp Schnittger[1,10,*]

[1]Department of Developmental Biology, Institute for Plant Sciences and Microbiology, University of Hamburg, Hamburg 22609, Germany
[2]Laboratoire de Reproduction et Développement des Plantes, Université de Lyon, ENS de Lyon, UCB Lyon 1, CNRS, INRAE, Lyon 69007, France
[3]Sainsbury Laboratory, University of Cambridge, Cambridge CB2 1LR, UK
[4]Department of Aquatic Ecophysiology and Phycology, Institute for Plant Sciences and Microbiology, University of Hamburg, Hamburg 22609, Germany
[5]Institute Jean-Pierre Bourgin, INRAE, AgroParisTech, Université Paris-Saclay, Versailles 78026, France
[6]Max-Planck-Institute for Plant Breeding Research, Cologne 50829, Germany
[7]Department of Plant Biotechnology and Bioinformatics, Ghent University, Ghent 9052, Belgium
[8]Vlaams Instituut voor Biotechnologie (VIB) Center for Plant Systems Biology, Ghent 9052, Belgium
[9]Present address: Department of Physics, Center for Biophysics, Saarland University, Saarbrücken 66123, Germany
[10]Lead contact
*Correspondence: francois.nedelec@slcu.cam.ac.uk (F.N.), arp.schnittger@uni-hamburg.de (A.S.)
https://doi.org/10.1016/j.devcel.2024.08.001

SUMMARY

To ensure an even segregation of chromosomes during somatic cell division, eukaryotes rely on mitotic spindles. Here, we measured prime characteristics of the *Arabidopsis* mitotic spindle and built a three-dimensional dynamic model using Cytosim. We identified the cell-cycle regulator CYCLIN-DEPENDENT KINASE B1 (CDKB1) together with its cyclin partner CYCB3;1 as key regulators of spindle morphology in *Arabidopsis*. We found that the augmin component ENDOSPERM DEFECTIVE1 (EDE1) is a substrate of the CDKB1;1-CYCB3;1 complex. A non-phosphorylatable mutant rescue of *ede1* resembled the spindle phenotypes of *cycb3;1* and *cdkb1* mutants and the protein associated less efficiently with spindle microtubules. Accordingly, reducing the level of augmin in simulations recapitulated the phenotypes observed in the mutants. Our findings emphasize the importance of cell-cycle-dependent phospho-control of the mitotic spindle in plant cells and support the validity of our model as a framework for the exploration of mechanisms controlling the organization of the eukaryotic spindle.

INTRODUCTION

Eukaryotes have acquired specific and robustly functioning cytoskeletal arrays to accomplish cell divisions. Plants in particular have unique microtubule arrays for cell division, namely the preprophase band (PPB), present in most plant cells, and the phragmoplast.[1] In somatic cells, the PPB forms in late-G2 cells committed to division and marks the future cortical cell-division site. After PPB disassembly and nuclear envelope breakdown (NEBD), a typical barrel-shaped spindle forms, which is responsible for the segregation of sister chromatids. In telophase, the phragmoplast appears, a cytokinetic array that drives centrifugal cell plate assembly and fusion to the parental cortex. Accurate regulation of the timing and architecture of each of these microtubule structures is essential for plant morphogenesis. While the PPB and the phragmoplast have been addressed in several studies leading to important insights about their organization, relatively little is known about the mechanisms driving assembly and function of the spindle of plant cells.

Most land plants form spindles in the absence of a distinct microtubule organizing center (MTOC), responsible for nucleating microtubules in a γ-tubulin-dependent manner. In animals, this MTOC is generally the centriole-containing centrosome.[2] γ-tubulin is part of the γ-tubulin ring complex (γTuRC) that acts as a template for microtubule polymerization.[3]

The augmin complex is a conserved γTuRC-targeting factor that is composed of eight members[4,5] and allows microtubule nucleation from existing microtubules, in a parallel or branched fashion.[5] Microtubule-dependent microtubule nucleation mediated by the augmin complex amplifies microtubule number while preserving their polarity.[6] In moss, it has been shown that knocking down augmin subunits leads to a reduction of around 50% in the number of spindle microtubules.[7] Hence, augmin activity is critical for microtubule amplification and organization in this plant spindle. In *Arabidopsis*, ENDOSPERM DEFECTIVE1 (EDE1), an AUG8/HAUS8 homolog, targets the whole complex to spindle microtubules during mitotic cell divisions.[8] A knockdown mutant of *EDE1* displays highly elongated spindles,

Please cite this article in press as: Romeiro Motta et al., The cell cycle controls spindle architecture in *Arabidopsis* by activating the augmin pathway, Developmental Cell (2024), https://doi.org/10.1016/j.devcel.2024.08.001

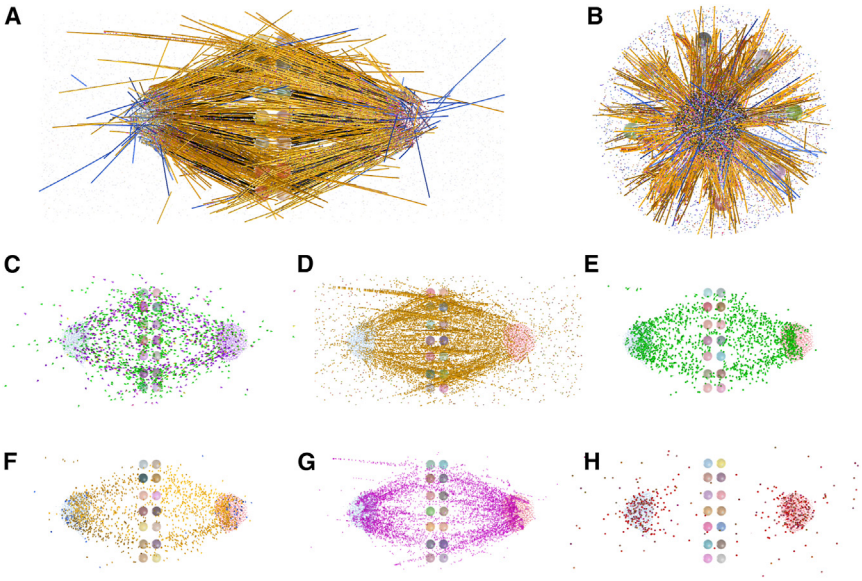

Figure 1. Tridimensional simulation of the *Arabidopsis* root mitotic spindle

(A and B) Snapshots of the simulations performed in Cytosim showing a side (A) and an end-on (B) view of the spindle. Microtubules are here color-coded according to the pathway of nucleation: blue if nucleated by the poles, black if nucleated by kinetochores, and yellow if nucleated by the augmin pathway. Chromosomes were not included in the model for simplicity, but 20 kinetochores were fixed in position such as to form a well-aligned metaphase plate. See also Figures S1 and S2 and Table S1 for more details.

(C–H) Distribution of key elements of the simulated spindle. (C) Microtubule plus ends (purple when shrinking and green when growing). (D) Kinesin-5 (yellow). (E) Augmin-activated nucleators (green). (F) Microtubule minus ends. (G) Kinesin-14 (pink). (H) Katanin (red).

whereas a null mutant of this gene results in lethality,[8,9] highlighting the role of the augmin complex in plant spindle architecture.

In human cells, Polo-like kinase 1 (Plk1) has been shown to promote the association of augmin-like complex subunit 8 (HAUS8, the human homolog of EDE1) with spindle microtubules.[10] However, plants lack Plk homologs, suggesting that cyclin-dependent kinase (CDK) complexes and/or Aurora kinases could take over some of their microtubule-associated functions in plants.[11,12] Indeed, cell-cycle factors like cyclins and CDKs are prime candidates for the regulation of spindle microtubules because of both their expression pattern as well as their localization.[13,14] In addition, plant CDK-cyclin complexes are known to be involved in the regulation of microtubule-associated proteins (MAPs) such as MAP65-1, whose interaction with microtubules is negatively regulated by CDK phosphorylation at prophase and metaphase.[15] Thus, there is strong evidence that CDK-cyclin phosphorylation is central for the organization and function of mitotic microtubule arrays, including the spindle.[16] Accordingly, B1-type cyclin double mutants (namely *cycb1;1 cycb1;2* and *cycb1;2 cycb1;3*) have spindles that show defects in chromosome capture, as well as other defects in the PPB and phragmoplast arrays.[17] However, little is known about the regulation of the spindle by CDK-cyclin complexes.

Here, we show that the B3-type cyclin of *Arabidopsis* and its main CDK partner CDKB1;1/CDKB1;2 control spindle morphogenesis. Remarkably, double *cdkb1;1 cdkb1;2* mutants displayed spindles with visible astral microtubules reminiscent of centrosome-derived microtubules observed in animal spindles. We identify EDE1, an augmin complex member homologous to AUG8, as a substrate of the CDKB1;1-CYCB3;1 complex. Moreover, we show that a non-phosphorylatable mutant form of EDE1 results in aberrant spindle length, and this phenotype is also seen in *cycb3;1* and *cdkb1;1 cdkb1;2* mutants. Similarly, reducing augmin concentration in a 3D model of the spindle results in elongated spindles, supporting our inference of the role of cell-cycle-dependent phosphorylation of augmin in plant cells.

RESULTS

Generation of a computational 3D simulation of the spindle

To understand the contribution of different molecular mechanisms to the organization of the spindle, we generated a three-dimensional dynamic model of an *Arabidopsis* root mitotic spindle using Cytosim, an open-source cytoskeleton simulation suite, that extends significantly over previous simulations of the *Xenopus* spindle (Figures 1A–1H, S1A–S1L, and S2A–S2G).[18,19] Microtubules were generated via three different pathways: directly nucleated at the kinetochores, nucleated by augmin on the side of pre-existing microtubules, and nucleated at the spindle poles, resulting in approximately 100, 1,500, and 100 microtubules in each pathway, respectively. These pathways shared a cellular pool of nucleators, and microtubule assembly was limited by the availability of tubulin in the cell. To simulate the spindle poles and anchor the microtubule fibers, we introduced a condensate with particle properties governed by smoothed particle hydrodynamics. In addition to augmin, we included kinesin-5,[20] kinesin-14,[21] and katanin[22] in our simulation. Kinesin-5 and kinesin-14 were added to promote microtubule cross-linking and spindle bipolarity by sliding microtubules apart and together, respectively. Notably, kinesin-5 was important to generate pulling forces on the kinetochores. Katanin was added to the condensate poles to regulate spindle length by severing. Dynein and Nuclear Mitotic Apparatus (NuMA) were excluded from our simulation due to their presumed absence in plants.[12] In addition, several simplifications were made, considering our focus on investigating how the general metaphase steady-state characteristics of the spindle are established. These include the fixation of kinetochores in a metaphase plate.

When possible, spindle parameters were determined experimentally (Figures S2H–S2Q). First, we estimated the number of spindle microtubules by analyzing transmission electron microscopy (TEM) images of cross-sections of *Arabidopsis* roots (Figures S2H and S2I). Second, the number of kinetochore

Please cite this article in press as: Romeiro Motta et al., The cell cycle controls spindle architecture in *Arabidopsis* by activating the augmin pathway, Developmental Cell (2024), https://doi.org/10.1016/j.devcel.2024.08.001

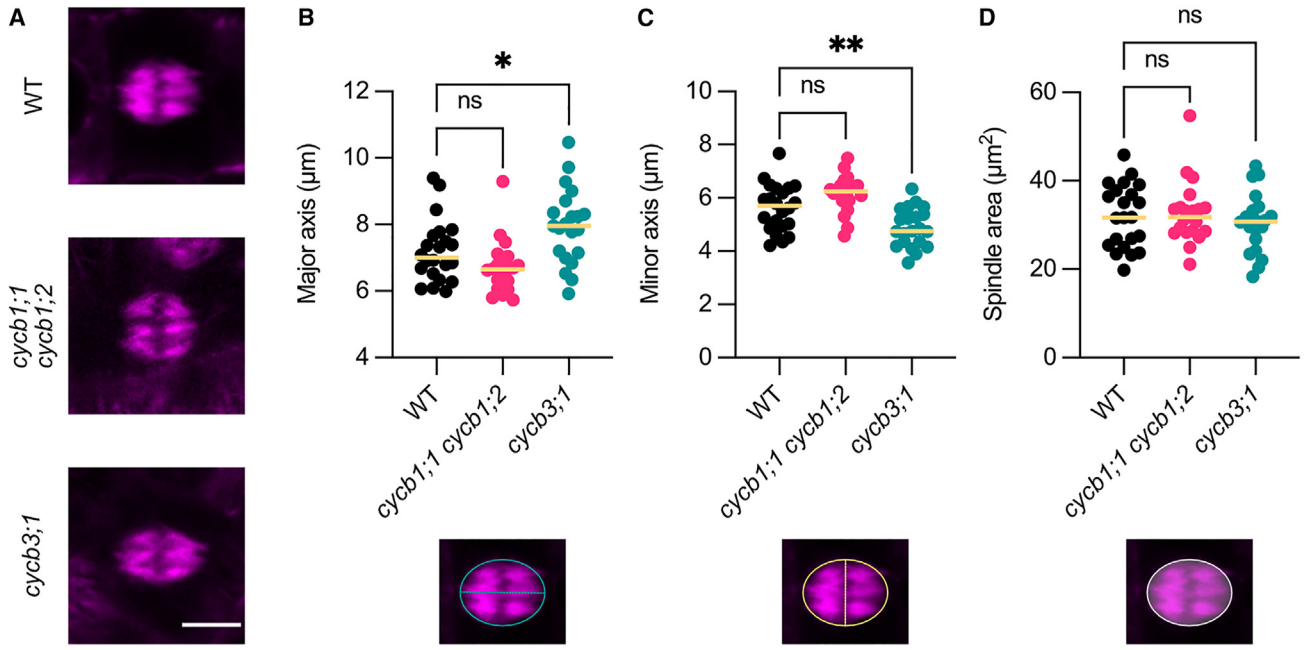

Figure 2. The *cycb3;1* mutant has an elongated spindle shape

(A) Confocal laser-scanning micrographs of TagRFP-TUA5-tagged microtubules in root cells at the spindle stage of WT, *cycb1;1 cycb1;2*, and *cycb3;1* plants. Scale bars, 5 µm.

(B–D) Quantification of the spindle major axis (B), minor axis (C), and area (D) in root cells of WT ($n = 22$), *cycb1;1 cycb1;2* ($n = 21$), and *cycb3;1* ($n = 21$) plants. Median values were plotted as a line for each genotype. The axis or region that was measured is indicated below each graph.

The level of significance was determined by an ordinary one-way ANOVA followed by Dunnett's multiple comparisons test (*$p < 0.05$ and **$p < 0.01$; ns depicts a non-significant difference). See also Table S2.

microtubules was estimated by measuring the fluorescence intensity of kinetochore fibers stained against α-tubulin and by counting the number of microtubules in bundles observed by TEM (Figures S2J–S2N). Third, the growth rate of microtubules was measured by using a reporter fusion for the end-binding protein 1 (EB1b; Figures S2O–S2Q).[23] A full list of the parameters used in the simulation is provided in Table S1.

Running this model produced organized spindles with focused poles and thick microtubule bundles that were attached in a bipolar manner to kinetochores (Figures 1A and 1B). Notably, we were able to closely reproduce the appearance of the barrel-shaped plant spindle with few pole-nucleated microtubules.

CYCLIN B3;1 controls spindle morphogenesis

To complement our simulation approach, we sought for possible cell-cycle regulators of the plant spindle. Since we have previously shown that mitotic B1-type cyclins are key regulators of microtubule organization in *Arabidopsis*,[17] we decided to assess spindle shape in roots of *cycb1;1 cycb1;2* double mutants (Figure 2A). This double-mutant combination has the strongest defects in growth and seed development among the B1-type cyclin mutant combinations, while still being viable.[17] We measured three spindle shape parameters, namely the lengths of major and minor axes and the area (Figures 2B–2D). Unexpectedly, the *cycb1;1 cycb1;2* mutant did not display any significant changes in spindle shape (Figures 2B–2D; Table S2).

We therefore hypothesized that other B-type cyclins could be involved in regulating spindle morphogenesis. The single member of the B3-type cyclin class in *Arabidopsis* was a good candidate as it was previously described to localize to the spindle in both mitosis and meiosis.[13,14] Indeed, spindles in roots of the *cycb3;1* mutant were more disc-shaped compared with the wild type (WT; Figure 2A)—the major axis was elongated and the minor axis was smaller, whereas the spindle area did not change significantly (Figures 2B–2D; Table S2). Thus, we concluded that CYCB3;1 is a regulator of spindle morphology in *Arabidopsis*.

CDKB1;1 is the main CDK partner of CYCB3;1, and the *cdkb1* mutant is hypersensitive to microtubule-destabilizing stress

To identify the main CDK partner(s) of CYCB3;1, as well as other potential interacting proteins and substrates, we performed affinity purification coupled to mass spectrometry (AP-MS) using CYCB3;1 as a bait in *Arabidopsis* cell suspension cultures (Figure 3A; Tables S3 and S4). Five proteins were identified as potential interactors of CYCB3;1 (Figure 3A). None of them, however, were directly involved in microtubule regulation. Enzyme-substrate interactions are known to be weak, and hence, it is not surprising that we did not detect good substrate candidates in this assay. The presence of CDKB1;1 among the potential interactors, however, suggested that this kinase is the main partner of CYCB3;1. Consistently, CYCB3;1 was previously found to co-purify with CDKB1;1 in tandem affinity purification experiments.[24]

CDKB1;1 was previously shown to play a role in controlling plant growth[25] and stomatal cell divisions.[26] CDKB1s are key

Please cite this article in press as: Romeiro Motta et al., The cell cycle controls spindle architecture in *Arabidopsis* by activating the augmin pathway, Developmental Cell (2024), https://doi.org/10.1016/j.devcel.2024.08.001

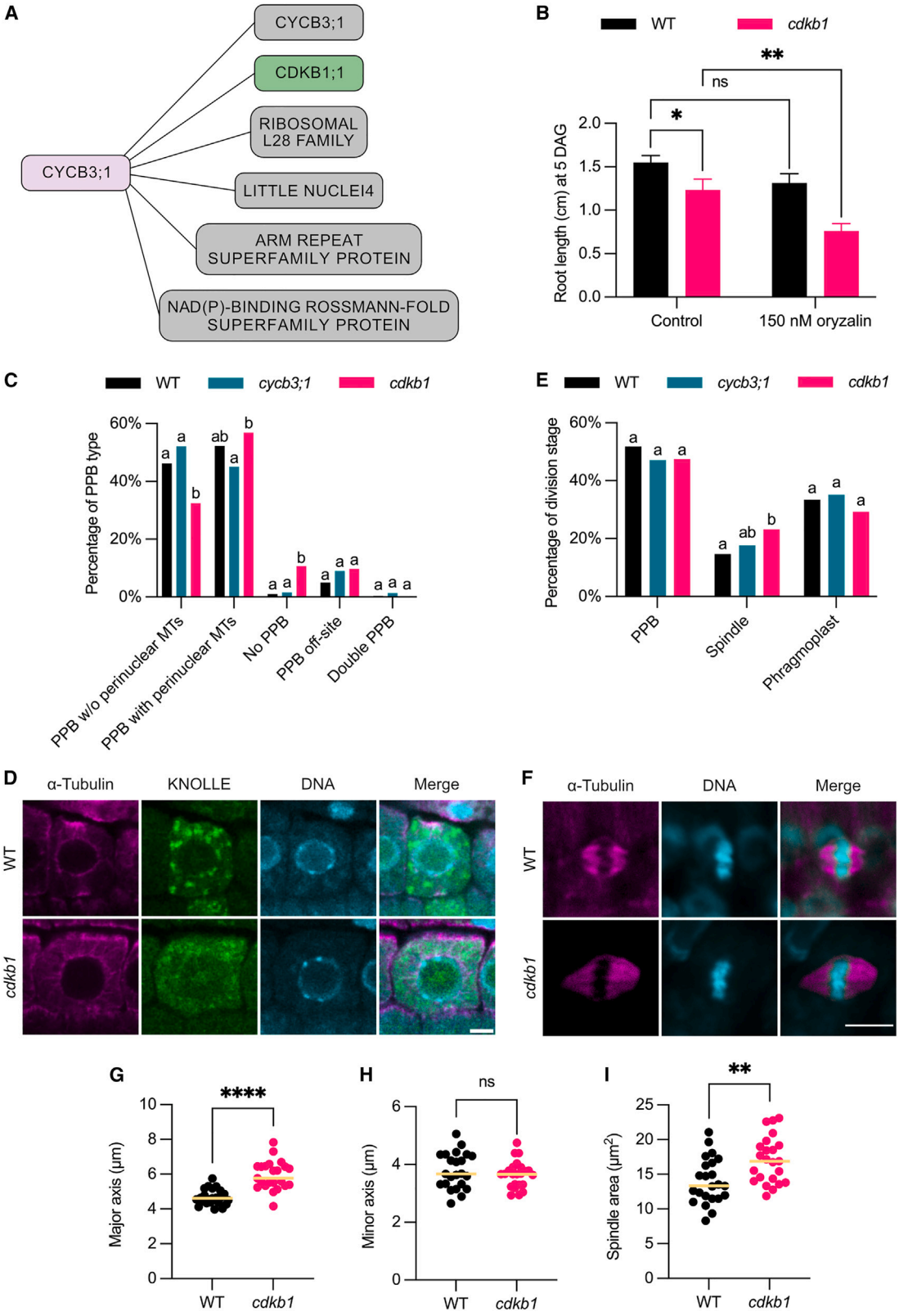

Figure 3. The *cdkb1* mutations affect PPB and spindle mitotic microtubule arrays

(A) Main protein interactors of CYCB3;1 as identified by AP-MS using CYCB3;1 as a bait. CDKB1;1 is highlighted in green, while other interactors that were not explored in this paper are shown in gray.

(legend continued on next page)

Please cite this article in press as: Romeiro Motta et al., The cell cycle controls spindle architecture in *Arabidopsis* by activating the augmin pathway, Developmental Cell (2024), https://doi.org/10.1016/j.devcel.2024.08.001

regulators of DNA damage response in *Arabidopsis*, e.g., in response to cisplatin, by activating homologous recombination repair.[27] CDKB1s have also been shown to play a minor and partially redundant role with CDKA;1,[28] and possibly other cell-cycle kinases, during cell proliferation and development of *Arabidopsis*. Remarkably, CDKB1;1 has also been identified at the spindle and phragmoplast arrays.[29] Because CDKB1;1 and CDKB1;2 have been found to function in a highly redundant manner and likely act in similar pathways,[27] we analyzed the double mutant for these two CDKs in the following experiments.

First, we decided to reassess the phenotype of the *cdkb1;1 cdkb1;2* double mutant (hereafter referred to as *cdkb1*, Figures 3B–3I). Initially, we analyzed root growth on oryzalin (Figure 3B). Oryzalin is a microtubule-destabilizing drug,[30] and many microtubule-related mutants are hypersensitive to this drug in comparison to the WT.[17] Under control conditions, the *cdkb1* mutant roots were 20.3% shorter than the WT 5 days after germination. Upon treatment with 150 nM oryzalin, *cdkb1* had a reduction of 38.5% in root growth, whereas, in the WT, the observed reduction in root growth was only marginally significant (Figure 3B). Thus, we concluded that the root growth phenotype of *cdkb1* is enhanced under mild microtubule destabilization conditions, prompting the hypothesis that CDKB1s could be involved in the control of mitotic microtubule arrays.

The *cdkb1* mutant displays PPB and spindle defects

To test the role of CDKB1s in controlling microtubule organization, we first performed whole-mount immunolocalization studies using antibodies against KNOLLE and α-tubulin as well as co-staining with DAPI for the DNA and counted the different mitotic stages (Figures 3C–3E; Table S5). KNOLLE staining allows the identification of G2/M cells where PPBs are normally present in the WT[31] (Figure S3). First, we found that, in *cdkb1*, 10.67% of KNOLLE-positive mitotic cells had no PPB, in comparison to only 1.01% in the WT (Figures 3C and 3D), indicating that *cdkb1* mutants have defects in the establishment of the PPB. Next, we found that the *cdkb1* double mutant had a higher frequency of mitotic cells at the spindle stage in their roots (23.21%) in comparison to the WT (14.70%; Figure 3E).

We then wondered if the spindle shape of the *cdkb1* double mutants was also altered. For this analysis, we measured the spindle shape as described above in whole-mount immunostained roots against α-tubulin and co-stained with DAPI (Figure 3F). Indeed, the spindles of *cdkb1* were significantly longer and larger in comparison to the WT (Figures 3F–3I; Table S2). Based on these findings, we concluded that CDKB1;1 is a major regulator of mitotic microtubule arrays, particularly at the PPB and spindle stages.

The *cycb3;1* and *cdkb1* mutants have an abnormal spindle organization and altered γ-tubulin distribution

To further characterize why the spindle shape was altered in *cycb3;1* and *cdkb1* mutants, we used super-resolution imaging with Airyscan (Figure 4). Spindles in *cdkb1* appeared highly disorganized in comparison to the WT, which could explain why they are bigger on average (Figures 3I and 4A). Furthermore, we noticed a striking number of astral microtubules in *cdkb1* spindles, which are essentially absent from the WT (Figures 4A–4C). In the *cdkb1* mutant, around half of the spindles (11 out of 23 spindles) had visible, generally short astral microtubules. This prompted us to check for the presence of astral microtubules in the *cycb3;1* mutant, and indeed, we also observed such microtubule configurations, albeit at a non-statistically significant frequency (2 out of 23 spindles; Figures 4A–4C). Nevertheless, these structures were never found in the WT ($n = 23$).

Next, given the central function of γ-tubulin in spindle organization and function,[32] we wondered if its distribution was affected in the *cycb3;1* and *cdkb1* mutants. To that end, we performed immunostaining against α- and γ-tubulin in cells of the root apical meristem of the *cycb3;1* and *cdkb1* mutants (Figures 4D–4F). The distribution of γ-tubulin, as expressed by the ratio of fluorescence peak distance divided by spindle length, was affected in both *cycb3;1* and *cdkb1* mutants compared with the WT (see STAR Methods and Figure 4F). Hence, we concluded that the localization of γ-tubulin in both *cycb3;1* and *cdkb1* mutants was strongly biased toward the spindle poles compared with the WT.

EDE1 is a substrate of the CDKB1;1-CYCB3;1 complex and its phosphorylation is important for its function

The spindle elongation phenotype found in *cycb3;1* and *cdkb1* mutants was reminiscent of the defects previously described in *ede1* mutants.[8] EDE1 is the microtubule-binding component of

(B) Quantification of root growth assays of WT and *cdkb1* seedlings on the control condition (DMSO) or 150 nM oryzalin. DAG, days after germination. Bars represent the mean value ± SD of three independent experiments with at least 16 plants per genotype per condition in each experiment. Comparisons on graph: WT control versus WT on oryzalin, $p = 0.0843$; WT control versus *cdkb1* control, $p = 0.0211$; *cdkb1* control versus *cdkb1* on oryzalin, $p = 0.0019$.
(C) Quantification of the different PPB types in the roots of WT, *cycb3;1*, and *cdkb1* plants. Different letters indicate significant differences in the proportion of the PPB type per category in a chi-squared test followed by the Marascuilo procedure to identify significant pairwise comparisons. Six roots were analyzed per genotype.
(D) Confocal laser-scanning micrographs of cells co-stained against α-tubulin (magenta) and KNOLLE (green) in the roots of WT and *cdkb1* plants. Nuclei were counterstained with DAPI for the DNA (cyan). At this stage, the WT shows a clear accumulation of KNOLLE and a PPB, whereas the *cdkb1* mutant shows an accumulation of KNOLLE but no obvious PPB. Scale bar, 5 μm.
(E) Quantification of PPB, spindle, and phragmoplast stages in the roots of WT, *cycb3;1*, and *cdkb1* plants. Different letters indicate significant differences in the proportion of the microtubule array per category in a chi-squared test followed by the Marascuilo procedure to identify significant pairwise comparisons. Six roots were analyzed per genotype.
(F) Confocal laser-scanning micrographs of root cells of WT and *cdkb1* plants at the spindle stage stained against α-tubulin (magenta) and counterstained for the DNA with DAPI (cyan). Scale bar, 5 μm.
(G–I) Quantification of the spindle major axis (G), minor axis (H), and area (I) in the root cells of WT and *cdkb1* plants ($n = 23$ for both genotypes). Median values were plotted as a line for each genotype.
The level of significance was determined by a two-way ANOVA followed by Tukey's multiple comparisons test in (B) and unpaired t tests in (G)–(I) (*$p < 0.05$, **$p < 0.01$, ****$p < 0.0001$; ns depicts a non-significant difference).
See also Figure S3 and Tables S2–S3, S4, and S5.

Please cite this article in press as: Romeiro Motta et al., The cell cycle controls spindle architecture in *Arabidopsis* by activating the augmin pathway, Developmental Cell (2024), https://doi.org/10.1016/j.devcel.2024.08.001

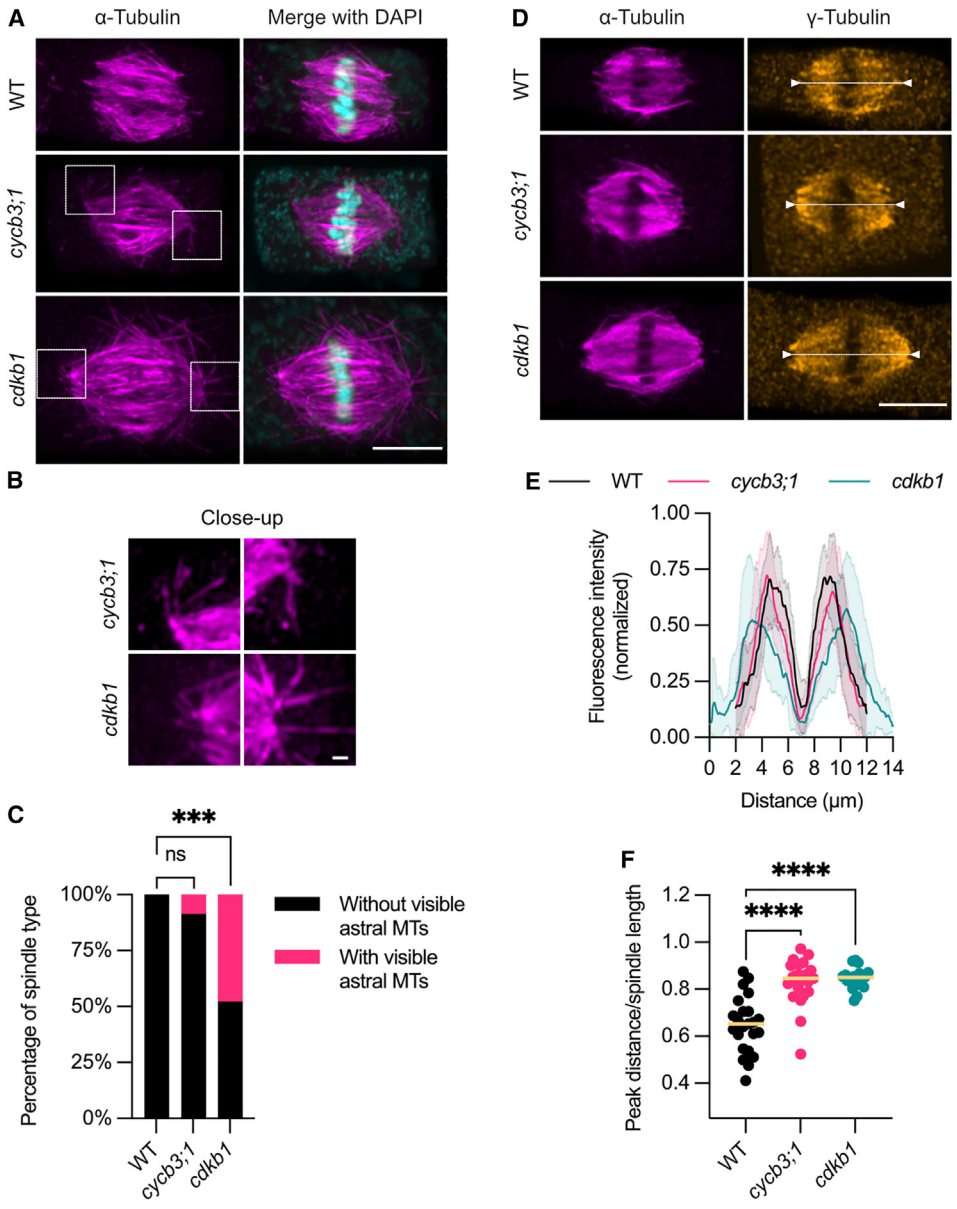

Figure 4. The *cycb3;1* and *cdkb1* mutants have spindles with visible astral microtubules

(A) Maximum intensity Z-projections of confocal laser-scanning micrographs of root cells of WT, *cycb3;1*, and *cdkb1* plants at the spindle stage stained against α-tubulin (magenta) and counterstained for the DNA with DAPI (cyan). The astral microtubules are highlighted with dashed white boxes. Scale bar, 5 μm.

(B) Close ups of the images shown in (A) depicting astral microtubules in the spindles of *cycb3;1* and *cdkb1* root cells stained against α-tubulin (magenta) and counterstained for the DNA with DAPI (cyan). Scale bar, 0.5 μm.

(C) Quantification of the number of spindles with or without visible astral microtubules in the root cells of WT, *cycb3;1*, and *cdkb1* plants ($n = 23$ for all genotypes).

(D) Single Z-slice confocal laser-scanning micrographs of root cells of WT, *cycb3;1*, and *cdkb1* plants at the spindle stage co-stained against α-tubulin (magenta) and γ-tubulin (orange). The white dashed line with the two arrowheads indicates the axis that was used to measure fluorescence intensity. Scale bar, 5 μm.

(E) Quantification of the fluorescence intensity of γ-tubulin across the spindle axis indicated in (D) in WT ($n = 23$), *cycb3;1* ($n = 23$), and *cdkb1* ($n = 22$) root cells.

(F) Quantification of the ratio of the distance between the fluorescence peaks seen in (E) divided by the spindle length value in WT (mean ± SD; 0.65 ± 0.12, $n = 23$), *cycb3;1* (0.83 ± 0.10, $n = 23$), and *cdkb1* (0.85 ± 0.04, $n = 22$) root cells. The median values were plotted as a line for each genotype. See STAR Methods for details. The level of significance was determined by a two-proportion z test followed by Bonferroni correction in (C) and an ordinary one-way ANOVA followed by Tukey's multiple comparisons test in (F) (***$p < 0.001$, ****$p < 0.0001$; ns depicts a non-significant difference).

the augmin complex in mitotic *Arabidopsis* cells. Additionally, the EDE1 protein contains eight CDK phosphorylation consensus (S-T/P) sites and was previously found to be phosphorylated by human Cdk1 in *in vitro* assays.[33] Hence, we tested if the CDKB1;1-CYCB3;1 complex could phosphorylate EDE1 *in vitro*. We found that EDE1 was phosphorylated at several sites, including but not limited to at least six of the eight CDK consensus phosphorylation sites (Figure 5A; Table S6).

Please cite this article in press as: Romeiro Motta et al., The cell cycle controls spindle architecture in *Arabidopsis* by activating the augmin pathway, Developmental Cell (2024), https://doi.org/10.1016/j.devcel.2024.08.001

CellPress
OPEN ACCESS

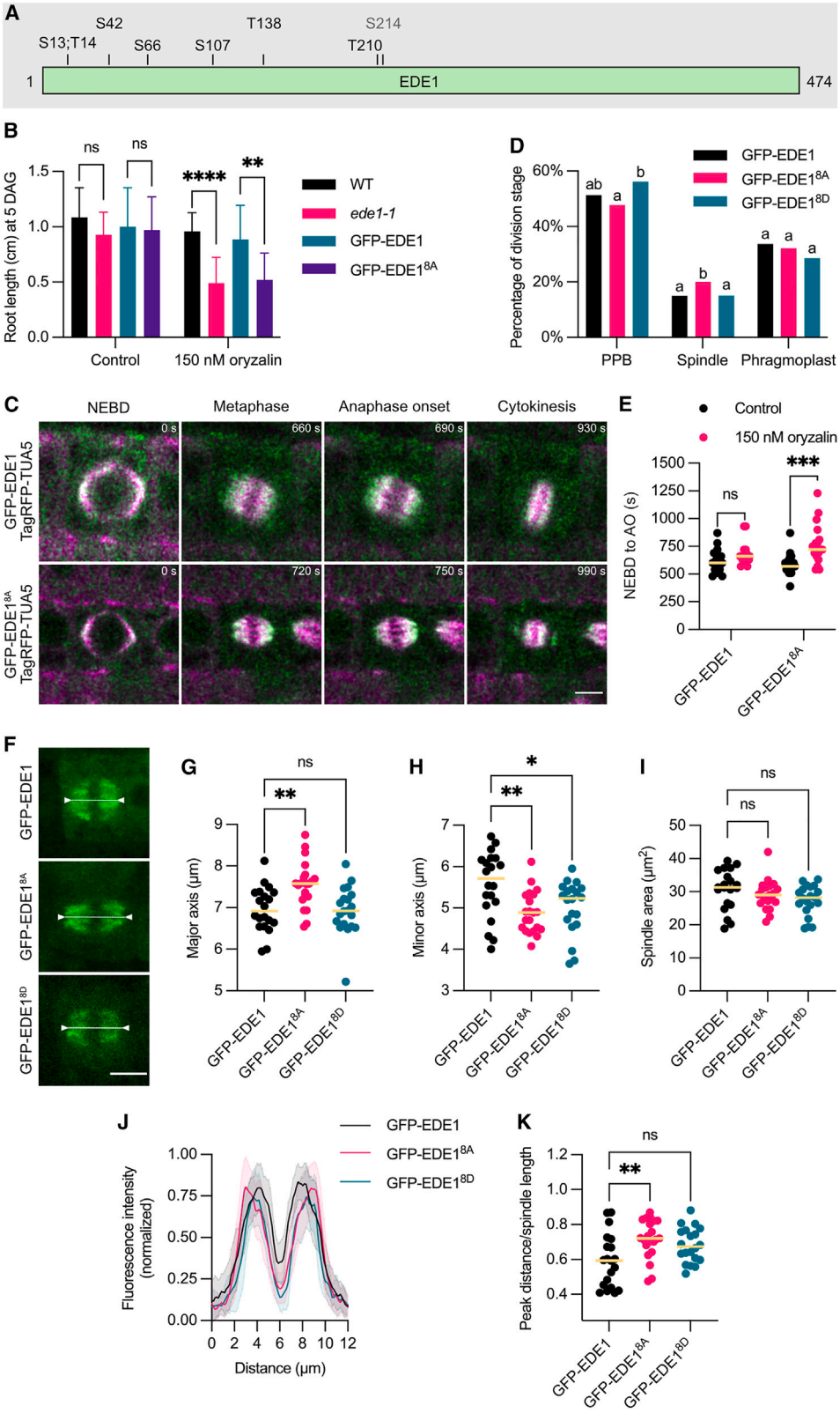

(legend on next page)

Please cite this article in press as: Romeiro Motta et al., The cell cycle controls spindle architecture in *Arabidopsis* by activating the augmin pathway, Developmental Cell (2024), https://doi.org/10.1016/j.devcel.2024.08.001

To address the localization of EDE1 in mitosis and assess the importance of its phosphorylation, we first generated a genomic EDE1 reporter (GFP-EDE1). We also mutated eight CDK phosphosites (seven of them identified *in vitro*) into either an alanine (GFP-EDE1^{8A}), which blocks phosphorylation, or an aspartate (GFP-EDE1^{8D}), which mimics a phosphorylated amino acid (Figure 5A). We introduced the WT and mutated versions in the knockdown *ede1-1* mutant background (hereafter referred to as *ede1*/GFP-EDE1, *ede1*/GFP-EDE1^{8A}, and *ede1*/GFP-EDE1^{8D}). The *ede1*/GFP-EDE1^{8A} plants had a fully rescued seed phenotype (Figures S4A and S4B). However, we found that their root growth was hypersensitive to oryzalin, similarly to the *ede1-1* mutant, whereas *ede1*/GFP-EDE1 plants grew similarly to the WT (Figures 5B and S4C). When we measured the timing from NEBD to anaphase onset (AO) with or without 150 nM oryzalin in *ede1*/GFP-EDE1 plants, we did not find a significant change (Figures 5C and 5E). By contrast, in *ede1*/GFP-EDE1^{8A} plants, the NEBD to AO duration was significantly longer in oryzalin-treated plants (Figures 5C and 5E). This showed that the functionality of the non-phosphorylatable GFP-EDE1^{8A} protein was affected, especially under stress conditions.

To further characterize mitotic defects in *ede1-1* plants rescued by the different GFP-EDE1 versions, we measured the frequency of PPB, spindle, and phragmoplast stages in root apical meristems (Figure 5D; Table S5). Similar to *cdkb1* mutants, *ede1*/GFP-EDE1^{8A} had a significant overrepresentation of spindle stages in mitotic cells (20.05% of total mitotic figures versus 14.99% in *ede1*/GFP-EDE1). We found that *ede1*/GFP-EDE1^{8A} plants displayed deformed spindles highly reminiscent of *cycb3;1* (Figures 5F–5I). Their major axis was larger and their minor axis was smaller in comparison to *ede1*/GFP-EDE1, whereas the spindle area did not change significantly (Table S2). Conversely, *ede1*/GFP-EDE1^{8D} did not have a significant change in the major axis or spindle area compared with *ede1*/GFP-EDE1, but still had a significantly smaller minor axis, albeit not as reduced as in *ede1*/GFP-EDE1^{8A} (Table S2). We concluded that EDE1 phosphorylation has an impact on spindle architecture under control conditions and becomes even more critical when microtubules are destabilized.

Based on the striking similarity between the phenotypes of *cycb3;1* and *ede1*/GFP-EDE1^{8A}, we hypothesized that EDE1 is a major substrate of CDK-cyclin complexes involving CYCB3;1. To test this hypothesis, we made crosses of *cycb3;1* with *ede1-1* mutants. Indeed, spindle defects in *cycb3;1 ede1-1* double mutants were identical to the single *ede1-1* mutant (Figures S4D–S4G). We thus concluded that EDE1 is the main substrate of CYCB3;1 action, whereas the *cdkb1* mutant phenotype is possibly more pleiotropic and a result of alterations in different CDK-cyclin phosphorylation pathways.

EDE1 phosphorylation is important for its localization at the spindle

Since the human homolog of EDE1 has been suggested to stabilize microtubules,[34] we wondered if *ede1*/GFP-EDE1^{8A} plants had impaired tubulin turnover,[35] which results from the combination of many microtubule activities including dynamic instability and could contribute to the above-described phenotypes. To test that, we performed fluorescence recovery after photobleaching (FRAP) assays of microtubules tagged with TagRFP-TUA5[36] in the *ede1*/GFP-EDE1 or *ede1*/GFP-EDE1^{8A}

Figure 5. EDE1 is a substrate of the CDKB1;1-CYCB3;1 complex and its phosphorylation is important for its function

(A) Representation of the protein sequence of EDE1. All of the eight mutated amino acids in the GFP-EDE1^{8A} and GFP-EDE1^{8D} constructs are represented alongside their amino acid position in the protein. Amino acids represented in black were found to be phosphorylated in the *in vitro* kinase assay with the CDKB1;1-CYCB3;1 complex, whereas the amino acid in gray (S214) was not identified in the *in vitro* kinase assay.

(B) Quantification of root growth assays of WT and *ede1-1* seedlings as well as *ede1-1* mutants rescued by GFP-EDE1 or GFP-EDE1^{8A} on the control condition (DMSO) or 150 nM oryzalin. Growth on the control (mean ± SD): WT 1.08 ± 0.27 cm; *ede1-1* 0.93 ± 0.20 cm; *ede1*/GFP-EDE1 1.00 ± 0.35 cm; and *ede1*/GFP-EDE1^{8A} 0.97 ± 0.30 cm. Growth on oryzalin (mean ± SD): WT 0.96 ± 0.17 cm; *ede1-1* 0.49 ± 0.23 cm; *ede1*/GFP-EDE1 0.88 ± 0.31 cm; and *ede1*/GFP-EDE1^{8A} 0.52 ± 0.24 cm. DAG, days after germination. Bars represent the mean ± SD (n = 12–24). Two other rescue lines in the *ede1-1* background were tested for both the GFP-EDE1 and GFP-EDE1^{8A} constructs with similar results.

(C) Confocal laser-scanning micrographs of GFP-EDE1- and TagRFP-TUA5-tagged microtubules in root cells of *ede1-1* mutants rescued by GFP-EDE1 and GFP-EDE1^{8A}. Mitotic cells were followed from nuclear envelope breakdown (NEBD) through the anaphase onset (AO) stage to cytokinesis. The time point is indicated on the top right of the images in seconds. Scale bar, 5 μm.

(D) Quantification of PPB, spindle, and phragmoplast stages in the roots of *ede-1* mutants rescued by GFP-EDE1, GFP-EDE1^{8A}, or GFP-EDE1^{8D}. Different letters indicate significant differences in the proportion of the microtubule array per category in a chi-squared test followed by the Marascuilo procedure to identify significant pairwise comparisons. Seven roots were analyzed per genotype.

(E) Quantification of the length of the NEBD to AO stage in root cells of *ede1-1* mutants rescued by GFP-EDE1 and GFP-EDE1^{8A} on the control (mean ± SD; 617.6 ± 104.0 s for GFP-EDE1 and 588.3 ± 98.8 s for GFP-EDE1^{8A}, n = 17–18) or 150 nM oryzalin condition (681.2 ± 102.7 s for GFP-EDE1 and 765.0 ± 180.7 s for GFP-EDE1^{8A}, n = 17–18). The median values were plotted as a line for each genotype and condition. Comparisons on graph: GFP-EDE1 control versus GFP-EDE1 on oryzalin, p = 0.4673; GFP-EDE1^{8A} control versus GFP-EDE1^{8A} on oryzalin, p = 0.0005.

(F) Confocal laser-scanning micrographs of GFP-EDE1-tagged microtubules in root cells at the spindle stage of *ede1-1* mutants rescued by GFP-EDE1, GFP-EDE1^{8A}, or GFP-EDE1^{8D}. Scale bar, 5 μm.

(G–I) Quantification of the spindle major axis (G), minor axis (H), and area (I) in the root cells of *ede1-1* mutants rescued by GFP-EDE1 (n = 20), GFP-EDE1^{8A} (n = 21), or GFP-EDE1^{8D} (n = 20). Median values were plotted as a line for each genotype.

(J) Quantification of the fluorescence intensity of GFP-EDE1 across the spindle axis indicated in (F) in root cells of *ede1-1* mutants rescued by GFP-EDE1 (n = 20), GFP-EDE1^{8A} (n = 21), or GFP-EDE1^{8D} (n = 20).

(K) Quantification of the ratio of the distance between the fluorescence peaks seen in (J) divided by the spindle length value in root cells of *ede1-1* mutants rescued by GFP-EDE1 (n = 20), GFP-EDE1^{8A} (n = 21), and GFP-EDE1^{8D} (n = 20). The median values were plotted as a line for each genotype. Comparisons on graph: GFP-EDE1 versus GFP-EDE1^{8A}, p = 0.0048; GFP-EDE1 versus GFP-EDE1^{8D}, p = 0.0610. See STAR Methods for details.

The level of significance was determined by a two-way ANOVA followed by Tukey's multiple comparisons test in (B) and one-way ANOVAs followed by Tukey's multiple comparisons tests in (E), (G)–(I), and (K) (*p < 0.05, **p < 0.01, ***p < 0.001, ****p < 0.0001; ns depicts a non-significant difference).

See also Figure S4 and Tables S2, S5, and S6.

backgrounds and observed their recovery over time (Figures S5A–S5F). However, we did not find a significant difference in the half-maximum values between the two genotypes, and fluorescence recovered at similar rates in both cases. Thus, we concluded that tubulin turnover did not change significantly in *ede1*/GFP-EDE1^{8A} plants in comparison to *ede1*/GFP-EDE1.

As EDE1 is known to recruit the γTuRC to spindle microtubules, and given the biased distribution of γ-tubulin in the *cycb3;1* and *cdkb1* mutants, we assessed the localization of the mutated forms of GFP-EDE1 at the spindle in the *ede1-1* background (Figures 5F, 5J, and 5K). Indeed, the distribution of GFP-EDE1^{8A} was significantly biased toward the spindle poles in comparison to GFP-EDE1, as expressed by the ratio of peak distance divided by spindle length, whereas the GFP-EDE1^{8D} version did not show a significant difference in localization in comparison to GFP-EDE1 (Figures 5F and 5K). In addition, we found that spindles of *ede1*/GFP-EDE1^{8A} and *ede1*/GFP-EDE1^{8D} plants also displayed visible astral microtubules at a low frequency (Figures 6A–6C), reminiscent of the *cycb3;1* mutant. Though the differences were not statistically significant regarding the proportion of spindles displaying astral microtubules in *ede1*/GFP-EDE1^{8A} or *ede1*/GFP-EDE1^{8D} in comparison to *ede1*/GFP-EDE1 (Figure 6C), we have shown above that these structures were never found in WT spindles (n = 23).

Since the binding of HAUS8 to microtubules is enhanced upon phosphorylation by Plk1,[10] we wondered if the phosphorylation of EDE1 also affects its association with microtubules. We thus performed FRAP assays in spindles of *ede1*/GFP-EDE1, *ede1*/GFP-EDE1^{8A}, and *ede1*/GFP-EDE1^{8D} root cells (Figures 6D–6F). The half maximum of GFP-EDE1^{8A} was on average 22.96 ± 10.42 s, significantly longer than GFP-EDE1 (12.04 ± 6.72 s). GFP-EDE1^{8D} had an average half maximum of 17.79 ± 8.78 s, further confirming that it functions more similarly to GFP-EDE1 than the GFP-EDE1^{8A} version, although this was still a significantly slower recovery compared with GFP-EDE1. Therefore, we concluded that the phosphorylation of EDE1 is important for its association with spindle microtubules and is significantly blocked in the GFP-EDE1^{8A} protein.

Altering the amount of augmin in the simulation affects spindle length and organization

To validate the role of augmin in overall spindle organization, and considering our experimental observations, we varied the amount of augmin in our simulations (Figures 7A–7I, n = 200 simulations of 1,000 s). Unexpectedly, we found a positive correlation between augmin source rate and spindle length for source rates smaller than 2/s, likely due to kinesin-5-mediated sliding of antiparallel microtubules. With more augmin, there are more microtubules that are able to bridge between the two sides of the spindle. Kinesin-5 can crosslink antiparallel microtubules, and as each head of kinesin-5 walks toward microtubules plus ends, it slides the antiparallel microtubules apart from each other, thus elongating the spindle. However, above a source rate of 2/s (while all other parameters were constant), spindle length decreased at an approximately constant rate (Figure 7A). In the range of augmin source rates we tested, the spindle length decreased by about 25%. With increasing augmin source rates, the average length of each kind of microtubule decreased, with augmin-nucleated microtubules experiencing the largest percentage decrease (almost 50%; Figure 7B). The number of augmin-nucleated microtubules increased from zero to more than 1,500, and the number of pole-nucleated microtubules decreased from around 150 to 50, while the number of kinetochore-nucleated microtubules remained approximately constant, as expected (Figure 7C). We also tested the effect of varying the augmin binding and nucleation rates on the spindle organization (Figure S6). Increasing binding and nucleation rates (Figures S6A–S6L) resulted in similar effects to increasing source rate.

DISCUSSION

In this work, we have combined computer simulations with experimental approaches to advance our knowledge of spindle formation in plants. We have identified CDKB1 in conjunction with CYCB3;1 as a major regulator of the *Arabidopsis* mitotic spindle. Until now, little was known in plants about how cell-cycle regulators control spindle formation. Based on their role in microtubule organization,[17] we had initially expected that B1-type cyclins, together with their CDK partners, mostly CDKB2s, would be involved in the regulation of spindle shape and organization. However, no obvious spindle defects were found in the most severe mutant combination *cycb1;1 cycb1;2*. Although we cannot rule out that other members of the B1 class participate in spindle architecture, CYCB1s seem mostly involved in other aspects of chromosome segregation, like the connection of spindle microtubules to kinetochores.[17] Accordingly, the B1-type cyclin from humans binds to and supports the localization of a member of the spindle assembly checkpoint (SAC), MAD1, at the kinetochore.[37] With respect to plant B1-type cyclins, it will be interesting to explore whether they have a similar role in regulating kinetochore proteins and/or the SAC, especially given that the core SAC machinery appears to be functionally conserved in *Arabidopsis*, albeit in an adapted manner.[38,39]

CDK-cyclin complexes have been previously implicated in the direct control of spindle morphogenesis in other organisms. For instance, the Cdk1-cyclin B1 complex from humans is known to phosphorylate importin-α1 to inhibit its function and release spindle assembly factors, such as Targeting protein for Xklp2 (TPX2), to promote spindle formation.[40] Furthermore, mutations in the budding yeast CDK1 (Cdc28) as well as simultaneous depletion of all budding yeast B-type cyclins also result in abnormal spindle assembly, which mirrors our findings with CYCB3;1 in *Arabidopsis*. More specifically, budding yeast cells impaired in Cdc28/B-cyclin function have duplicated spindle pole bodies (SPBs) that fail to separate.[41] The Cdc28/B-cyclin complex specifically phosphorylates yeast kinesins-5 Kip1 and Cin8, and this phosphorylation plays a role in promoting SPB separation and spindle assembly.[42] Although plants lack a discernable MTOC at the spindle stage like SPBs or centrosomes, here we found that γ-tubulin (a major component of SPBs and centrosomes) distribution is likewise impaired in *cycb3;1* and *cdkb1* mutants. In *Arabidopsis*, no less than 23 kinesins are expressed in mitosis, among which many have potential CDK phosphosites.[43] Whether B-type cyclins are involved in the phospho-control of such mitotic kinesins and help establish spindle bipolarity in plant cells remains to be seen.

Please cite this article in press as: Romeiro Motta et al., The cell cycle controls spindle architecture in *Arabidopsis* by activating the augmin pathway, Developmental Cell (2024), https://doi.org/10.1016/j.devcel.2024.08.001

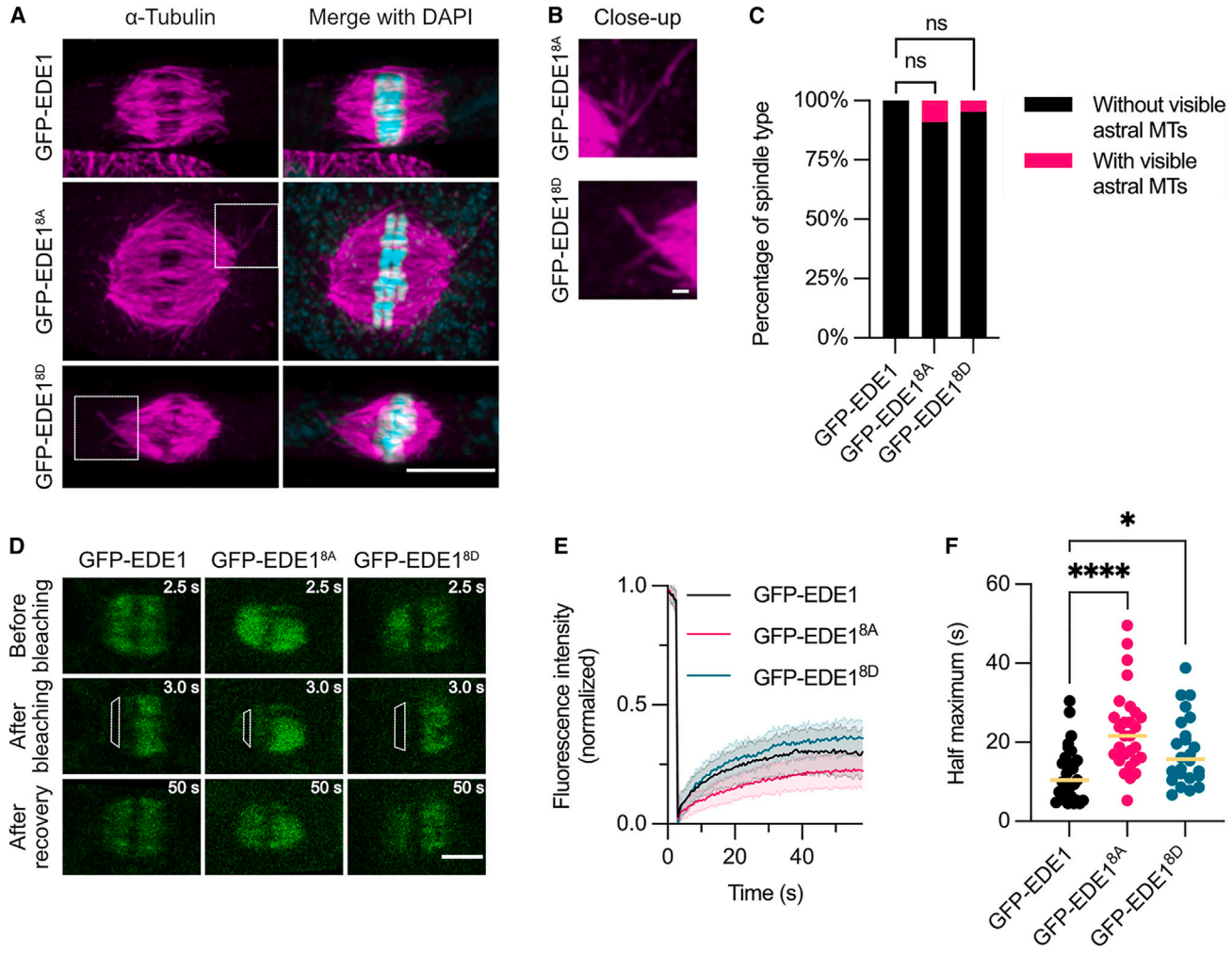

Figure 6. The phosphorylation of EDE1 is important for its localization at spindle microtubules

(A) Maximum intensity Z-projections of confocal laser-scanning micrographs of root cells of *ede1-1* mutants rescued by GFP-EDE1, GFP-EDE1^{8A}, and GFP-EDE1^{8D} at the spindle stage stained against α-tubulin (magenta) and counterstained for the DNA with DAPI (cyan). The astral microtubules are highlighted with dashed white boxes. Scale bar, 5 μm.

(B) Close ups of the images shown in (A) depicting astral microtubules in the spindles of *ede1-1* mutant root cells rescued by GFP-EDE1^{8A} and GFP-EDE1^{8D} and stained against α-tubulin (magenta) and counterstained for the DNA with DAPI (cyan). Scale bar, 0.5 μm.

(C) Quantification of spindles with or without visible astral microtubules in the root cells of *ede1-1* mutants rescued by GFP-EDE1 (n = 12), GFP-EDE1^{8A} (n = 22), and GFP-EDE1^{8D} (n = 21).

(D) Confocal laser-scanning micrographs of root cells in which the FRAP assay of spindles tagged by GFP-EDE1, GFP-EDE1^{8A}, or GFP-EDE1^{8D} in the *ede1-1* background was performed. The white dashed box represents the area that was bleached by the laser. The time is indicated on the top right of the images in seconds. Scale bar, 5 μm.

(E) Quantification of the fluorescence intensity recovery over time following bleaching of spindles in root cells tagged by GFP-EDE1 (n = 31), GFP-EDE1^{8A} (n = 28), or GFP-EDE1^{8D} (n = 24) in the *ede1-1* background. The fluorescence intensity was normalized in each cell by the maximum and minimum values and plotted as an average (line) ± SD (shaded area).

(F) Quantification of the half-maximum values in seconds of fluorescence recovery in *ede1-1* mutants rescued by GFP-EDE1 (n = 31), GFP-EDE1^{8A} (n = 28), or GFP-EDE1^{8D} (n = 24). The median values were plotted as a line for each genotype. Comparisons on graph: GFP-EDE1 versus GFP-EDE1^{8A}, $p < 0.0001$; GFP-EDE1 versus GFP-EDE1^{8D}, $p = 0.0452$.

The level of significance was determined by a two-proportion z test followed by Bonferroni correction in (C) and an ordinary one-way ANOVA followed by Tukey's multiple comparisons test in (F) (*$p < 0.05$, ****$p < 0.0001$; ns depicts a non-significant difference).

The role of CDKB1 and CYCB3;1 in spindle organization

Here, we found that the CYCB3;1-CDKB1 complex is involved in spindle morphogenesis, at least partly through phospho-regulation of the augmin complex member EDE1. Interestingly, tubulin turnover does not seem to be affected in the non-phosphorylatable version of EDE1 we analyzed; hence, we propose that the elongated spindle phenotype we observed is mostly due to an altered frequency and/or pattern of microtubule-dependent microtubule nucleation within the spindle. If tubulin availability in a cell limits spindle length, spindles can become longer when augmin function is affected because the amount of free tubulin increases, as does the polymerization speed of the

Please cite this article in press as: Romeiro Motta et al., The cell cycle controls spindle architecture in *Arabidopsis* by activating the augmin pathway, Developmental Cell (2024), https://doi.org/10.1016/j.devcel.2024.08.001

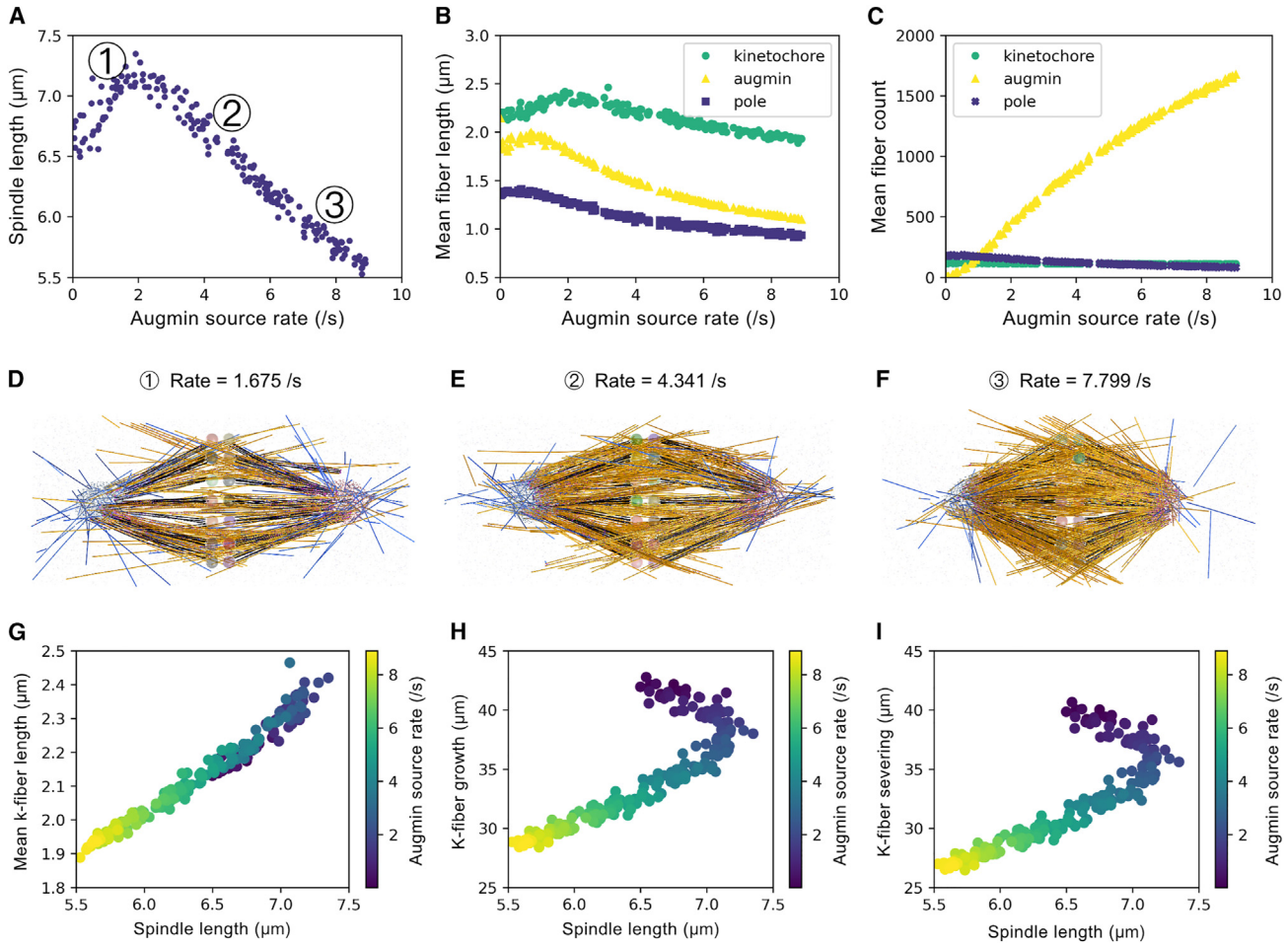

Figure 7. The amount of augmin controls spindle length and organization in the simulation

(A–C) Some key spindle properties as a function of the augmin source rate (/s). All temporal means are taken over the last half of the simulation, 500 s < t < 1,000 s.

(A) The mean spindle length (μm) decreases with augmin source rate (/s). The spindle length is measured as the distance between the center-of-masses of the left and right groups of condensate beads. The numbers indicate the three examples shown in (D)–(F).

(B) Mean lengths (μm) of each group of fibers nucleated at kinetochores (green circles), by augmin (yellow triangles), and at poles (purple squares).

(C) Mean number of fibers of each type.

(D–F) Visualization of simulated spindles at the final time t = 1,000 s, for augmin source rates as indicated. Kinetochore microtubules are black, augmin-nucleated microtubules are yellow, and pole-nucleated microtubules are blue. Kinetochores are variously colored spheres near the metaphase plate.

(G–I) Relationships between kinetochore-fiber (k-fiber) properties and the spindle length (μm), with data points colored according to the augmin source rate (/s). All quantities are means over the last half of the simulation, 500 s < t < 1,000 s, and k-fiber quantities are averaged over all k-fibers. (G) Mean k-fiber length (μm), (H) mean growth (μm) at k-fiber plus ends, and (I) mean severing (μm) at k-fiber minus ends.

See also Figure S6.

remaining spindle microtubules. Indeed, in our simulations, spindles became shorter in response to increasing augmin source rate. As the augmin source rate increased from 2.711/s to 8.891/s, the amount of free tubulin (measured as the microtubule length equivalent) decreased from 2,500 to 1,800 μm. With an augmin source rate of 2.711/s, the actual microtubule growth speed was about 40% lower than the base microtubule growth speed, whereas with a source rate of 8.891/s, the growth speed was reduced by about 55%. Consequently, kinetochore microtubules became shorter, contributing to shortening the spindle (Figures 7G–7I). Furthermore, pole-nucleated microtubules were longer and more abundant with lower levels of augmin in our simulations, fitting our observation of a higher and more visible number of astral microtubules in *cdkb1* mutants. Perhaps parallel nucleation and other augmin-independent nucleation pathways become more common in the mutants we studied, further contributing to the change in spindle shape we observed as previously suggested for the *ede1-1* mutant.[8] Additionally, since the augmin complex nucleates microtubules that generally preserve the polarity of their mother microtubules,[6] the astral microtubules in *cycb3;1* and *cdkb1* represent further evidence of a deficient augmin activity. Possibly contributing to the elongated spindle phenotype we observed is the antagonism of augmin toward katanin.[44] The accumulation of augmin at the spindle poles could hypothetically reduce katanin-mediated severing of microtubules.

Please cite this article in press as: Romeiro Motta et al., The cell cycle controls spindle architecture in *Arabidopsis* by activating the augmin pathway, Developmental Cell (2024), https://doi.org/10.1016/j.devcel.2024.08.001

Why do *cycb3;1* and *cdkb1* mutants display spindles with an altered distribution of γ-tubulin, biased toward the poles? At the prophase stage, the pro-spindle is present normally as two polar caps rich in γ-tubulin at the nuclear envelope,[45] and this structure seems unperturbed in the analyzed mutants. Following NEBD, augmin has been shown to critically bind to and amplify the number of microtubules to assist spindle formation.[12] Augmin likely translocates γ-tubulin from the spindle poles (which form from remnants of the polar caps following NEBD) toward spindle microtubules in the midzone. In the *cycb3;1* and *cdkb1* mutants, however, a faulty augmin-mediated redistribution of γ-tubulin upon NEBD likely results in the accumulation of γ-tubulin at the spindle poles.

Since the spindle defects seen in *cdkb1* double mutants are stronger than in *cycb3;1* mutants, it seems probable that CDKB1s operate with other cyclins to control spindle morphology. CDKB1s may also be involved in the establishment of the cortical division site, since we often observed cells without a PPB in *cdkb1* mutants (Figures 3C and 3D), although we did not examine this further. Interestingly, phragmoplasts were normal in the mutants we analyzed. This indicates that augmin may be activated by other kinases or other CDK-cyclin complexes at this stage, considering that CYCB3;1 has been degraded by the end of the spindle stage.[13,14]

Basic molecular mechanisms guiding spindle organization

Here, we have modeled a spindle in three dimensions with increased realism in comparison to previous work and including additional factors such as augmin and kinesin-14.[19,46] Whereas a quantitatively accurate model of the *Xenopus* spindle has not yet been achieved due to its size, the smaller size of the *Arabidopsis* spindle meant it was possible to simulate all of its microtubules within a reasonable computational time. Modeling an *Arabidopsis* mitotic spindle in particular was interesting because it has an intermediate size that is ideal for simulations when compared with smaller fission yeast or larger *Xenopus laevis* spindles and because plant spindles lack key molecular players seen in animals. For instance, there is only limited evidence of a NuMA homolog in plants,[12,47] and hence, the pole organization in our simulation differs from the NuMA-organized spindle poles that have previously been employed.[19,46] Plants also lack the molecular motor dynein, which was also not included in our simulation, but possess an astonishing number of kinesins, including several expressed in mitosis, that likely take over some of dynein's functions.[48]

With this work, we shed light on molecular mechanisms governing spindle organization in plants that are likely relevant for other eukaryotic groups as well. Our simulation will serve as a foundation for understanding spindle organization in other species, thus advancing our knowledge of how cells ensure a robustly functioning spindle structure to separate their chromosomes in cell divisions and thereby proliferate.

Limitations of the study

In our spindle simulations, some simplifications were made. For instance, we fixed kinetochores in place, and many numerical parameters we employed cannot currently be determined experimentally or are difficult to obtain. However, we were still able to closely reproduce the mitotic *Arabidopsis* spindle. In the future, as we learn more about the structural, biochemical, and biophysical features of eukaryotic spindles, it will likely be possible to simulate spindles that more closely represent the complexity of these structures in cells.

Regarding our experiments, we cannot rule out that EDE1 is also phosphorylated by other kinases other than the CDKB1; 1-CYCB3;1 complex or that this complex phosphorylates other MAPs in cells that also contribute to the observed spindle phenotypes. Nevertheless, there is a striking similarity in the phenotypes of *cycb3;1* and *ede1*/GFP-EDE1^{8A} spindles. This, together with the data obtained in the *cycb3;1 ede1* double mutant, represents convincing evidence that CYCB3;1-containing CDK-cyclins complexes are great contributors to EDE1 phosphorylation. Furthermore, although we did not find a difference in tubulin turnover between *ede1*/GFP-EDE1 and *ede1*/GFP-EDE1^{8A}, there are likely slight changes in microtubule organization or dynamics that were not detected with our FRAP experiment. Thus, it would be interesting to study the structure and dynamics of these spindles with better spatial and temporal resolution.

STAR★METHODS

Detailed methods are provided in the online version of this paper and include the following:

- KEY RESOURCES TABLE
- RESOURCE AVAILABILITY
  - Lead contact
  - Materials availability
  - Data and code availability
- EXPERIMENTAL MODEL AND STUDY PARTICIPANT DETAILS
  - Plant growth conditions
- METHOD DETAILS
  - Arabidopsis root mitotic spindle simulation
  - TEM of Arabidopsis root cross-sections
  - AP-MS on CYCB3;1
  - Root growth assays and timing of mitotic divisions on oryzalin
  - Wholemount immunolocalization of α-tubulin and KNOLLE in roots
  - Immunolocalization of α- and γ-tubulin in root meristematic cells
  - Protein expression and purification and *in vitro* kinase assay
  - Sample preparation and LC-MS/MS data acquisition for the identification of EDE1 phosphosites
  - MS data analysis and PRM method development
  - Generation of the GFP-EDE1 reporter
  - FRAP assay
- QUANTIFICATION AND STATISTICAL ANALYSIS
  - Experimental determination of spindle parameters
  - Spindle morphogenesis image analysis
  - Root growth assays on oryzalin
  - Wholemount immunolocalization of α-tubulin and KNOLLE in roots
  - FRAP assay
  - Statistical software

SUPPLEMENTAL INFORMATION

Supplemental information can be found online at https://doi.org/10.1016/j.devcel.2024.08.001.

ACKNOWLEDGMENTS

We thank Dr. Roland Thünauer for technical support at the Advanced Light and Fluorescence Microscopy facility at the CSSB (DESY, Hamburg), Anne Harzen at the MPI for Plant Breeding Research for liquid chromatography-tandem mass spectrometry (LC-MS/MS) analysis in the identification of EDE1

phosphosites, and the VIB Proteomics Core for the LC-MS/MS analysis of the AP-MS samples. We thank the Cambridge Research Computing services, specifically for high performance computing used for this study. This work was supported by the HFSP grant RGP0023/2018 to A.S. and D.B.; F.N., H.S., and C.J. were supported by the Gatsby Charitable Foundation (Grant PTAG-024) and the European Research Council (ERC Synergy Grant, project 951430).

AUTHOR CONTRIBUTIONS

M.R.M. and A.S. conceived the experiments. F.N., H.S., and C.J. constructed the spindle simulations and analyzed them. E.W. fixed and processed plant samples for TEM and performed TEM imaging. M.P., K.B., and D.B. performed the whole-mount immunolocalization of α-tubulin and KNOLLE and corresponding statistical analyses. S.C.S. and H.N. performed the mass spectrometry experiment and data analysis of the *in vitro* kinase assays. E.V.D.S. and G.D.J. performed the AP-MS of CYCB3;1 and corresponding statistical analyses. M.R.M. and L.B. performed all other experiments and statistical analyses. M.R.M. and A.S. analyzed the data. M.R.M. and A.S. wrote the manuscript with input from all authors.

DECLARATION OF INTERESTS

The authors declare no competing interests.

Received: November 14, 2023
Revised: May 25, 2024
Accepted: August 5, 2024
Published: August 26, 2024

REFERENCES

1. Romeiro Motta, M., and Schnittger, A. (2021). A microtubule perspective on plant cell division. Curr. Biol. *31*, R547–R552. https://doi.org/10.1016/j.cub.2021.03.087.
2. Petry, S., and Vale, R.D. (2015). Microtubule nucleation at the centrosome and beyond. Nat. Cell Biol. *17*, 1089–1093. https://doi.org/10.1038/ncb3220.
3. Teixidó-Travesa, N., Roig, J., and Lüders, J. (2012). The where, when and how of microtubule nucleation – one ring to rule them all. J. Cell Sci. *125*, 4445–4456. https://doi.org/10.1242/jcs.106971.
4. Goshima, G., Mayer, M., Zhang, N., Stuurman, N., and Vale, R.D. (2008). Augmin: A protein complex required for centrosome-independent microtubule generation within the spindle. J. Cell Biol. *181*, 421–429. https://doi.org/10.1083/jcb.200711053.
5. Sánchez-Huertas, C., and Lüders, J. (2015). The augmin connection in the geometry of microtubule networks. Curr. Biol. *25*, R294–R299. https://doi.org/10.1016/j.cub.2015.02.006.
6. Alfaro-Aco, R., Thawani, A., and Petry, S. (2020). Biochemical reconstitution of branching microtubule nucleation. eLife *9*, e49797. https://doi.org/10.7554/eLife.49797.
7. Nakaoka, Y., Miki, T., Fujioka, R., Uehara, R., Tomioka, A., Obuse, C., Kubo, M., Hiwatashi, Y., and Goshima, G. (2012). An inducible RNA interference system in *Physcomitrella patens* reveals a dominant role of augmin in phragmoplast microtubule generation. Plant Cell *24*, 1478–1493. https://doi.org/10.1105/tpc.112.098509.
8. Lee, Y.J., Hiwatashi, Y., Hotta, T., Xie, T., Doonan, J.H., and Liu, B. (2017). The mitotic function of augmin is dependent on its microtubule-associated protein subunit EDE1 in *Arabidopsis thaliana*. Curr. Biol. *27*, 3891–3897.e4. https://doi.org/10.1016/j.cub.2017.11.030.
9. Pignocchi, C., Minns, G.E., Nesi, N., Koumproglou, R., Kitsios, G., Benning, C., Lloyd, C.W., Doonan, J.H., and Hills, M.J. (2009). ENDOSPERM DEFECTIVE1 is a novel microtubule-associated protein essential for seed development in *Arabidopsis*. Plant Cell *21*, 90–105. https://doi.org/10.1105/tpc.108.061812.
10. Johmura, Y., Soung, N.K., Park, J.E., Yu, L.R., Zhou, M., Bang, J.K., Kim, B.Y., Veenstra, T.D., Erikson, R.L., and Lee, K.S. (2011). Regulation of microtubule-based microtubule nucleation by mammalian polo-like kinase 1. Proc. Natl. Acad. Sci. USA *108*, 11446–11451. https://doi.org/10.1073/pnas.1106223108.
11. De Cárcer, G., Manning, G., and Malumbres, M. (2011). From Plk1 to Plk5: functional evolution of polo-like kinases. Cell Cycle *10*, 2255–2262. https://doi.org/10.4161/cc.10.14.16494.
12. Yamada, M., and Goshima, G. (2017). Mitotic spindle assembly in land plants: molecules and mechanisms. Biology (Basel) *6*, 6. https://doi.org/10.3390/biology6010006.
13. Sofroni, K., Takatsuka, H., Yang, C., Dissmeyer, N., Komaki, S., Hamamura, Y., Böttger, L., Umeda, M., and Schnittger, A. (2020). CDKD-dependent activation of CDKA;1 controls microtubule dynamics and cytokinesis during meiosis. J. Cell Biol. *219*, e201907016. https://doi.org/10.1083/jcb.201907016.
14. Bulankova, P., Akimcheva, S., Fellner, N., and Riha, K. (2013). Identification of Arabidopsis meiotic cyclins reveals functional diversification among plant cyclin genes. PLoS Genet. *9*, e1003508. https://doi.org/10.1371/journal.pgen.1003508.
15. Smertenko, A.P., Chang, H.Y., Sonobe, S., Fenyk, S.I., Weingartner, M., Bögre, L., and Hussey, P.J. (2006). Control of the AtMAP65-1 interaction with microtubules through the cell cycle. J. Cell Sci. *119*, 3227–3237. https://doi.org/10.1242/jcs.03051.
16. Liu, B., and Lee, Y.J. (2022). Spindle assembly and mitosis in plants. Annu. Rev. Plant Biol. *73*, 227–254. https://doi.org/10.1146/annurev-arplant-070721-084258.
17. Romeiro Motta, M., Zhao, X., Pastuglia, M., Belcram, K., Roodbarkelari, F., Komaki, M., Harashima, H., Komaki, S., Kumar, M., Bulankova, P., et al. (2022). B1-type cyclins control microtubule organization during cell division in *Arabidopsis*. EMBO Rep. *23*, e53995. https://doi.org/10.15252/embr.202153995.
18. Nedelec, F., and Foethke, D. (2007). Collective Langevin dynamics of flexible cytoskeletal fibers. New J. Phys. *9*, 427. https://doi.org/10.1088/1367-2630/9/11/427.
19. Loughlin, R., Wilbur, J.D., McNally, F.J., Nédélec, F.J., and Heald, R. (2011). Katanin contributes to interspecies spindle length scaling in *Xenopus*. Cell *147*, 1397–1407. https://doi.org/10.1016/j.cell.2011.11.014.
20. Mann, B.J., and Wadsworth, P. (2019). Kinesin-5 regulation and function in mitosis. Trends Cell Biol. *29*, 66–79. https://doi.org/10.1016/j.tcb.2018.08.004.
21. She, Z.Y., and Yang, W.X. (2017). Molecular mechanisms of kinesin-14 motors in spindle assembly and chromosome segregation. J. Cell Sci. *130*, 2097–2110. https://doi.org/10.1242/jcs.200261.
22. Kuo, Y.W., and Howard, J. (2021). Cutting, amplifying, and aligning microtubules with severing enzymes. Trends Cell Biol. *31*, 50–61. https://doi.org/10.1016/j.tcb.2020.10.004.
23. Komaki, S., Abe, T., Coutuer, S., Inzé, D., Russinova, E., and Hashimoto, T. (2010). Nuclear-localized subtype of end-binding 1 protein regulates spindle organization in *Arabidopsis*. J. Cell Sci. *123*, 451–459. https://doi.org/10.1242/jcs.062703.
24. Van Leene, J., Hollunder, J., Eeckhout, D., Persiau, G., Van De Slijke, E., Stals, H., Van Isterdael, G., Verkest, A., Neirynck, S., Buffel, Y., et al. (2010). Targeted interactomics reveals a complex core cell cycle machinery in *Arabidopsis thaliana*. Mol. Syst. Biol. *6*, 397. https://doi.org/10.1038/msb.2010.53.
25. Boudolf, V., Vlieghe, K., Beemster, G.T.S., Magyar, Z., Torres Acosta, J.A., Maes, S., Van Der Schueren, E., Inzé, D., and De Veylder, L. (2004). The plant-specific cyclin-dependent kinase CDKB1;1 and transcription factor E2Fa-DPa control the balance of mitotically dividing and endoreduplicating cells in Arabidopsis. Plant Cell *16*, 2683–2692. https://doi.org/10.1105/tpc.104.024398.
26. Xie, Z., Lee, E., Lucas, J.R., Morohashi, K., Li, D., Murray, J.A.H., Sack, F.D., and Grotewold, E. (2010). Regulation of cell proliferation in the stomatal lineage by the *Arabidopsis* MYB FOUR LIPS via direct targeting of

core cell cycle genes. Plant Cell *22*, 2306–2321. https://doi.org/10.1105/tpc.110.074609.

27. Weimer, A.K., Biedermann, S., Harashima, H., Roodbarkelari, F., Takahashi, N., Foreman, J., Guan, Y., Pochon, G., Heese, M., Van Damme, D., et al. (2016). The plant-specific CDKB1-CYCB1 complex mediates homologous recombination repair in *Arabidopsis*. EMBO J. *35*, 2068–2086. https://doi.org/10.15252/embj.201593083.
28. Nowack, M.K., Harashima, H., Dissmeyer, N., Zhao, X., Bouyer, D., Weimer, A.K., De Winter, F., Yang, F., and Schnittger, A. (2012). Genetic framework of cyclin-dependent kinase function in *Arabidopsis*. Dev. Cell *22*, 1030–1040. https://doi.org/10.1016/j.devcel.2012.02.015.
29. Boruc, J., Mylle, E., Duda, M., de Clercq, R., Rombauts, S., Geelen, D., Hilson, P., Inzé, D., van Damme, D., and Russinova, E. (2010). Systematic localization of the Arabidopsis core cell cycle proteins reveals novel cell division complexes. Plant Physiol. *152*, 553–565. https://doi.org/10.1104/pp.109.148643.
30. Hugdahl, J.D., and Morejohn, L.C. (1993). Rapid and reversible high-affinity binding of the dinitroaniline herbicide oryzalin to tubulin from *Zea mays* L. Plant Physiol. *102*, 725–740. https://doi.org/10.1104/pp.102.3.725.
31. Spinner, L., Gadeyne, A., Belcram, K., Goussot, M., Moison, M., Duroc, Y., Eeckhout, D., De Winne, N., Schaefer, E., Van De Slijke, E., et al. (2013). A protein phosphatase 2A complex spatially controls plant cell division. Nat. Commun. *4*, 1863. https://doi.org/10.1038/ncomms2831.
32. Pastuglia, M., Azimzadeh, J., Goussot, M., Camilleri, C., Belcram, K., Evrard, J.L., Schmit, A.C., Guerche, P., and Bouchez, D. (2006). γ-tubulin is essential for microtubule organization and development in *Arabidopsis*. Plant Cell *18*, 1412–1425. https://doi.org/10.1105/tpc.105.039644.
33. Pignocchi, C., and Doonan, J.H. (2011). Interaction of a 14-3-3 protein with the plant microtubule-associated protein EDE1. Ann. Bot. *107*, 1103–1109. https://doi.org/10.1093/aob/mcr050.
34. Wu, G., Lin, Y.-T., Wei, R., Chen, Y., Shan, Z., and Lee, W.-H. (2008). Hice1, a novel microtubule-associated protein required for maintenance of spindle integrity and chromosomal stability in human cells. Mol. Cell. Biol. *28*, 3652–3662. https://doi.org/10.1128/MCB.01923-07.
35. Omelyanchuk, L.V., and Munzarova, A.F. (2017). Theoretical model of mitotic spindle microtubule growth for FRAP curve interpretation. BMC Syst. Biol. *11*, 378. https://doi.org/10.1186/s12918-016-0378-9.
36. Prusicki, M.A., Keizer, E.M., van Rosmalen, R.P., Komaki, S., Seifert, F., Müller, K., Wijnker, E., Fleck, C., and Schnittger, A. (2019). Live cell imaging of meiosis in Arabidopsis thaliana. eLife *8*, 1–31. https://doi.org/10.7554/eLife.42834.
37. Allan, L.A., Camacho Reis, M., Ciossani, G., Huis In 't Veld, P.J., Wohlgemuth, S., Kops, G.J., Musacchio, A., and Saurin, A.T. (2020). Cyclin B1 scaffolds MAD1 at the kinetochore corona to activate the mitotic checkpoint. EMBO J. *39*, e103180. https://doi.org/10.15252/embj.2019103180.
38. Komaki, S., and Schnittger, A. (2017). The spindle assembly checkpoint in *Arabidopsis* is rapidly shut off during severe stress. Dev. Cell *43*, 172–185.e5. https://doi.org/10.1016/j.devcel.2017.09.017.
39. Komaki, S., and Schnittger, A. (2016). The spindle checkpoint in plants — a green variation over a conserved theme? Curr. Opin. Plant Biol. *34*, 84–91. https://doi.org/10.1016/j.pbi.2016.10.008.
40. Guo, L., Mohd, K.S., Ren, H., Xin, G., Jiang, Q., Clarke, P.R., and Zhang, C. (2019). Phosphorylation of importin-α1 by CDK1-cyclin B1 controls mitotic spindle assembly. J. Cell Sci. *132*, jcs232314. https://doi.org/10.1242/jcs.232314.
41. Haase, S.B., Winey, M., and Reed, S.I. (2001). Multi-step control of spindle pole body duplication by cyclin-dependent kinase. Nat. Cell Biol. *3*, 38–42. https://doi.org/10.1038/35050543.
42. Chee, M.K., and Haase, S.B. (2010). B-Cyclin/CDKs regulate mitotic spindle assembly by phosphorylating kinesins-5 in budding yeast. PLoS Genet. *6*, e1000935. https://doi.org/10.1371/journal.pgen.1000935.
43. Vanstraelen, M., Inzé, D., and Geelen, D. (2006). Mitosis-specific kinesins in *Arabidopsis*. Trends Plant Sci. *11*, 167–175. https://doi.org/10.1016/j.tplants.2006.02.004.
44. Wang, G., Wang, C., Liu, W., Ma, Y., Dong, L., Tian, J., Yu, Y., and Kong, Z. (2018). Augmin antagonizes katanin at microtubule crossovers to control the dynamic organization of plant cortical arrays. Curr. Biol. *28*, 1311–1317.e3. https://doi.org/10.1016/j.cub.2018.03.007.
45. Lee, Y.J., and Liu, B. (2019). Microtubule nucleation for the assembly of acentrosomal microtubule arrays in plant cells. New Phytol. *222*, 1705–1718. https://doi.org/10.1111/nph.15705.
46. Loughlin, R., Heald, R., and Nédélec, F. (2010). A computational model predicts *Xenopus* meiotic spindle organization. J. Cell Biol. *191*, 1239–1249. https://doi.org/10.1083/jcb.201006076.
47. Yu, W., and Moreno Díaz De La Espina, S. (1999). The plant nucleoskeleton: ultrastructural organization and identification of NuMa homologues in the nuclear matrix and mitotic spindle of plant cells. Exp. Cell Res. *246*, 516–526. https://doi.org/10.1006/excr.1998.4334.
48. Reddy, A.S.N., and Day, I.S. (2001). Kinesins in the Arabidopsis genome: A comparative analysis among eukaryotes. BMC Genomics *2*, 2. https://doi.org/10.1186/1471-2164-2-2.
49. Lauber, M.H., Waizenegger, I., Steinmann, T., Schwarz, H., Mayer, U., Hwang, I., Lukowitz, W., and Jürgens, G. (1997). The *Arabidopsis* KNOLLE protein is a cytokinesis-specific syntaxin. J. Cell Biol. *139*, 1485–1493. https://doi.org/10.1083/jcb.139.6.1485.
50. Harashima, H., and Schnittger, A. (2012). Robust reconstitution of active cell-cycle control complexes from co-expressed proteins in bacteria. Plant Methods *8*, 23. https://doi.org/10.1186/1746-4811-8-23.
51. Schindelin, J., Arganda-Carreras, I., Frise, E., Kaynig, V., Longair, M., Pietzsch, T., Preibisch, S., Rueden, C., Saalfeld, S., Schmid, B., et al. (2012). Fiji: an open-source platform for biological-image analysis. Nat. Methods *9*, 676–682. https://doi.org/10.1038/nmeth.2019.
52. Cox, J., and Mann, M. (2008). MaxQuant enables high peptide identification rates, individualized p.p.b.-range mass accuracies and proteome-wide protein quantification. Nat. Biotechnol. *26*, 1367–1372. https://doi.org/10.1038/nbt.1511.
53. MacLean, B., Tomazela, D.M., Shulman, N., Chambers, M., Finney, G.L., Frewen, B., Kern, R., Tabb, D.L., Liebler, D.C., and MacCoss, M.J. (2010). Skyline: an open source document editor for creating and analyzing targeted proteomics experiments. Bioinformatics *26*, 966–968. https://doi.org/10.1093/bioinformatics/btq054.
54. Clough, S.J., and Bent, A.F. (1998). Floral dip: a simplified method for Agrobacterium-mediated transformation of *Arabidopsis thaliana*. Plant J. *16*, 735–743. https://doi.org/10.1046/j.1365-313X.1998.00343.x.
55. Daniels, B.R., Masi, B.C., and Wirtz, D. (2006). Probing single-cell micromechanics in vivo: the microrheology of *C. elegans* developing embryos. Biophys. J. *90*, 4712–4719. https://doi.org/10.1529/biophysj.105.080606.
56. Kraus, J., Travis, S.M., King, M.R., and Petry, S. (2023). Augmin is a Ran-regulated spindle assembly factor. J. Biol. Chem. *299*, 104736. https://doi.org/10.1016/j.jbc.2023.104736.
57. Carazo-Salas, R.E., Guarguaglini, G., Gruss, O.J., Segref, A., Karsenti, E., and Mattaj, I.W. (1999). Generation of GTP-bound ran by RCC1 is required for chromatin-induced mitotic spindle formation. Nature *400*, 178–181. https://doi.org/10.1038/22133.
58. Heald, R., Tournebize, R., Blank, T., Sandaltzopoulos, R., Becker, P., Hyman, A., and Karsenti, E. (1996). Self-organization of microtubules into bipolar spindles around artificial chromosomes in *Xenopus* egg extracts. Nature *382*, 420–425. https://doi.org/10.1038/382420a0.
59. David, A.F., Roudot, P., Legant, W.R., Betzig, E., Danuser, G., and Gerlich, D.W. (2019). Augmin accumulation on long-lived microtubules drives amplification and kinetochore-directed growth. J. Cell Biol. *218*, 2150–2168. https://doi.org/10.1083/jcb.201805044.
60. Brun, L., Rupp, B., Ward, J.J., and Nédélec, F. (2009). A theory of microtubule catastrophes and their regulation. Proc. Natl. Acad. Sci. USA *106*, 21173–21178. https://doi.org/10.1073/pnas.0910774106.

61. Dogterom, M., and Yurke, B. (1997). Measurement of the force-velocity relation for growing microtubules. Science *278*, 856–860. https://doi.org/10.1126/science.278.5339.856.

62. van den Wildenberg, S.M.J.L., Tao, L., Kapitein, L.C., Schmidt, C.F., Scholey, J.M., and Peterman, E.J.G. (2008). The homotetrameric kinesin-5 KLP61F preferentially crosslinks microtubules into antiparallel orientations. Curr. Biol. *18*, 1860–1864. https://doi.org/10.1016/j.cub.2008.10.026.

63. Heck, M.M., Pereira, A., Pesavento, P., Yannoni, Y., Spradling, A.C., and Goldstein, L.S. (1993). The kinesin-like protein KLP61F is essential for mitosis in Drosophila. J. Cell Biol. *123*, 665–679. https://doi.org/10.1083/jcb.123.3.665.

64. Monaghan, J.J. (1992). Smoothed particle hydrodynamics. Annu. Rev. Astron. Astrophys. *30*, 543–574. https://doi.org/10.1146/annurev.aa.30.090192.002551.

65. Desbrun, M., and Gascuel, M.-P. (1996). Smoothed particles: a new paradigm for animating highly deformable bodies. In Proceedings of the Eurographics workshop on Computer animation and simulation '96,, pp. 61–76. https://doi.org/10.1007/978-3-7091-7486-9_5.

66. Akinci, N., Akinci, G., and Teschner, M. (2013). Versatile surface tension and adhesion for SPH fluids. ACM Trans. Graph. *32*, 1–8. https://doi.org/10.1145/2508363.2508395.

67. Brugués, J., Nuzzo, V., Mazur, E., and Needleman, D.J. (2012). Nucleation and transport organize microtubules in metaphase spindles. Cell *149*, 554–564. https://doi.org/10.1016/j.cell.2012.03.027.

68. Spurr, A.R. (1969). A low-viscosity epoxy resin embedding medium for electron microscopy. J. Ultrastruct. Res. *26*, 31–43. https://doi.org/10.1016/s0022-5320(69)90033-1.

69. Reynolds, E.S. (1963). The use of lead citrate at high pH as an electron-opaque stain in electron microscopy. J. Cell Biol. *17*, 208–212. https://doi.org/10.1083/jcb.17.1.208.

70. Van Leene, J., Eeckhout, D., Cannoot, B., De Winne, N., Persiau, G., Van De Slijke, E., Vercruysse, L., Dedecker, M., Verkest, A., Vandepoele, K., et al. (2015). An improved toolbox to unravel the plant cellular machinery by tandem affinity purification of *Arabidopsis* protein complexes. Nat. Protoc. *10*, 169–187. https://doi.org/10.1038/nprot.2014.199.

71. Van Leene, J., Eeckhout, D., Gadeyne, A., Matthijs, C., Han, C., De Winne, N., Persiau, G., Van De Slijke, E., Persyn, F., Mertens, T., et al. (2022). Mapping of the plant SnRK1 kinase signalling network reveals a key regulatory role for the class II T6P synthase-like proteins. Nat. Plants *8*, 1245–1261. https://doi.org/10.1038/s41477-022-01269-w.

72. Liu, B., Marc, J., Joshi, H.C., and Palevitz, B.A. (1993). A γ-tubulin-related protein associated with the microtubule arrays of higher plants in a cell cycle-dependent manner. J. Cell Sci. *104*, 1217–1228. https://doi.org/10.1242/jcs.104.4.1217.

73. Rappsilber, J., Ishihama, Y., and Mann, M. (2003). Stop and Go Extraction tips for matrix-assisted laser desorption/ionization, nanoelectrospray, and LC/MS sample pretreatment in proteomics. Anal. Chem. *75*, 663–670. https://doi.org/10.1021/ac026117i.

74. Perez-Riverol, Y., Bai, J., Bandla, C., García-Seisdedos, D., Hewapathirana, S., Kamatchinathan, S., Kundu, D.J., Prakash, A., Frericks-Zipper, A., Eisenacher, M., et al. (2022). The PRIDE database resources in 2022: a hub for mass spectrometry-based proteomics evidences. Nucleic Acids Res. *50*, D543–D552. https://doi.org/10.1093/nar/gkab1038.

75. Herrmann, A., Livanos, P., Zimmermann, S., Berendzen, K., Rohr, L., Lipka, E., and Müller, S. (2021). KINESIN-12E regulates metaphase spindle flux and helps control spindle size in Arabidopsis. Plant Cell *33*, 27–43. https://doi.org/10.1093/plcell/koaa003.

Please cite this article in press as: Romeiro Motta et al., The cell cycle controls spindle architecture in *Arabidopsis* by activating the augmin pathway, Developmental Cell (2024), https://doi.org/10.1016/j.devcel.2024.08.001

STAR★METHODS

KEY RESOURCES TABLE

REAGENT or RESOURCE	SOURCE	IDENTIFIER
Antibodies		
Mouse monoclonal anti-α-Tubulin	Sigma-Aldrich	Cat#T9026; RRID: AB_477593
Mouse monoclocal anti-γ-Tubulin	Agrisera	Cat#AS20 4482
Mouse monoclonal anti-α-Tubulin	Sigma-Aldrich	Cat#T5168; RRID: AB_477579
Rabbit anti-KNOLLE	Lauber et al.[49]	N/A
Goat anti-mouse STAR 580	Abberior	Cat#ST580-1001-500UG; RRID: AB_2923543
Goat anti-mouse STAR 635P	Abberior	Cat#ST635P-1001-500UG; RRID: AB_2893232
Goat anti-rabbit Alexa Fluor 555	Thermo Fisher Scientific	Cat#A-21428; RRID: AB_2535849
Goat anti-mouse Alexa Fluor 488	Thermo Fischer Scientific	Cat#A-11001; RRID: AB_2534069
Bacterial and virus strains		
E. coli TOP10	Thermo Fisher Scientific	Cat#C404010
Agrobacterium tumefaciens strain GV3101	N/A	N/A
E. coli BL21 (DE3) pLysS	Thermo Fisher Scientific	Cat#C606003
Critical commercial assays		
Gateway BP Clonase II Enzyme mix	Thermo Fisher Scientific	Cat#11789020
Gateway LR Clonase II Enzyme mix	Thermo Fisher Scientific	Cat# 11791020
Deposited data		
Mass spectrometry proteomics data	This paper	PRIDE: PXD046697
Source code for simulations in Cytosim	This paper	Zenodo: 10.5281/zenodo.12209363
Experimental models: Organisms/strains		
Arabidopsis thaliana: Col-0 (Wild type)	NASC	N1093
Arabidopsis thaliana: *cycb1;1*	Weimer et al.[27]	N/A
Arabidopsis thaliana: *cycb1;2*	Weimer et al.[27]	N/A
Arabidopsis thaliana: *cycb3;1*	Bulankova et al.[14]	WiscDsLox461-464I10
Arabidopsis thaliana: *cdkb1;1*	Nowack et al.[28]	SALK_073457
Arabidopsis thaliana: *cdkb1;2*	Nowack et al.[28]	SALK_133560
Arabidopsis thaliana: *ede1-1*	NASC, Pignocchi et al.[9]	N9868
Arabidopsis thaliana: PRO_{RPS5A}*:TagRFP:TUA5* in Col-0	Prusicki et al.[36]	N/A
Arabidopsis thaliana: PRO_{RPS5A}*:TagRFP:TUA5* in *cycb1;1 cycb1;2*	This paper	N/A
Arabidopsis thaliana: PRO_{RPS5A}*:TagRFP:TUA5* in *cycb3;1*	Sofroni et al.[13]	N/A
Arabidopsis thaliana: PRO_{EDE1}*:GFP:EDE1* in *ede1-1*	This paper	N/A
Arabidopsis thaliana: PRO_{EDE1}*:GFP:EDE1*^{8A} in *ede1-1*	This paper	N/A
Arabidopsis thaliana: PRO_{EDE1}*:GFP:EDE1*^{8D} in *ede1-1*	This paper	N/A
Arabidopsis thaliana: PRO_{EDE1}*:GFP:EDE1/* PRO_{RPS5A}*:TagRFP:TUA5* in *ede1-1*	This paper	N/A
Arabidopsis thaliana: PRO_{EDE1}*:GFP:EDE1*^{8A}*/* PRO_{RPS5A}*:TagRFP:TUA5* in *ede1-1*	This paper	N/A
Arabidopsis thaliana: PRO_{EB1b}*:EB1b:GFP* in Col-0	Komaki et al.[23]	N/A
Arabidopsis thaliana: PRO_{RPS5A}*:TagRFP:TUA5* in *ede1-1*	This paper	N/A
Arabidopsis thaliana: PRO_{RPS5A}*:TagRFP:TUA5* in *cycb3;1 ede1-1*	This paper	N/A
Oligonucleotides		
Primers used in this study are listed in Table S7	This paper	N/A

(*Continued on next page*)

Please cite this article in press as: Romeiro Motta et al., The cell cycle controls spindle architecture in *Arabidopsis* by activating the augmin pathway, Developmental Cell (2024), https://doi.org/10.1016/j.devcel.2024.08.001

Continued

REAGENT or RESOURCE	SOURCE	IDENTIFIER
Recombinant DNA		
PRO_{RPS5A}:TagRFP:TUA5	Prusicki et al.[36]	N/A
PRO_{EDE1}:GFP:EDE1	This paper	N/A
PRO_{EDE1}:GFP:EDE1^{8A}	This paper	N/A
PRO_{EDE1}:GFP:EDE1^{8D}	This paper	N/A
pHGGWA/HisGST-EDE1	This paper	N/A
pHMGWA/HisMBP-CYCB3;1	Sofroni et al.[13]	N/A
pCDFDuet-1/StrepIII-CDKB1;1	Harashima and Schnittger[50]	N/A
Software and algorithms		
Fiji	Schindelin et al.[51]	https://imagej.net/Fiji
Cytosim	Nedelec and Foethke[18]	https://gitlab.com/f-nedelec/cytosim
Mascot	N/A	https://www.matrixscience.com/
MaxQuant	Cox and Mann[52]	https://www.maxquant.org/
Skyline	MacLean et al.[53]	https://skyline.ms

RESOURCE AVAILABILITY

Lead contact

Further information and requests for resources and reagents should be directed to and will be fulfilled by the lead contact, Arp Schnittger (arp.schnittger@uni-hamburg.de).

Materials availability

Further information and requests for resources and reagents listed in the key resources table should be directed to the lead contact.

Data and code availability

- Mass spectrometry proteomics data that were used to identify EDE1 phosphosites have been deposited to the ProteomeXchange Consortium via the PRIDE partner repository and are publicly available as of the date of publication. The DOI is listed in the key resources table. Microscopy and any other data reported in this paper will be shared by the lead contact upon request.
- All original code for the spindle simulations has been deposited at Zenodo and is publicly available as of the date of publication. The DOI is listed in the key resources table.
- Any additional information required to reanalyze the data reported in this paper is available from the lead contact upon request.

EXPERIMENTAL MODEL AND STUDY PARTICIPANT DETAILS

Plant growth conditions

Arabidopsis thaliana seeds were grown on ½ MS medium (basal salt mixture, Duchefa Biochemie) containing 0.5% sucrose and 0.8% agar (plant agar, Duchefa Biochemia). Seeds were initially sterilized with a solution containing 2% bleach and 0.05% Triton X-100 for 5 min followed by three washes with sterile distilled water and the addition of 0.05% agarose. Plates with seeds were then stratified at 4°C for 2–3 days in the dark. Next, plates were placed in an *in vitro* growth chamber at a temperature of 22°C in a 16-hour light regime. Seedlings were transferred afterwards to soil in a growth chamber with a 16-hour/21°C light and 8-hour/18°C dark regime with 60% humidity. Plants were transformed using the floral dipping method.[54]

METHOD DETAILS

Arabidopsis root mitotic spindle simulation

Mitotic spindles were simulated using Cytosim, an Open-Source project (gitlab.com/f-nedelec/cytosim). Here, we provide an overview of our methods, which are based on Brownian dynamics. The numerical aspects (integration, stability) were described previously.[18] Further to this publication, accessibility of the source code should enable the full analysis of our methods and reproducibility of the results. While some parameters are provided below, the configuration file for Cytosim is the only definitive source for parameter values. In brief, microtubules are modeled as incompressible bendable filaments having the persistence length of microtubules, in a medium characterized by a viscosity as measured for cells.[55] Microtubules are represented by vertices distributed regularly along their length. Connections between microtubules and forces, such as steric interactions, are represented by Hookean links between

the filament's vertices. The forces are linearly interpolated to adjacent vertices on the filament when a link is formed between two vertices. The evolution of the entire network is simulated by solving the equation of motion for successive small-time intervals, updating this equation as the motors move to different positions on the filaments, and motor and crosslinkers bind or unbind, and microtubules grow, shrink, vanish, or are created. In essence, the movement is defined by an over-damped Langevin equation: $\xi \frac{dx}{dt} = f(x,t) + B(t)$, for a large multivariate vector x, where the right-hand terms are elastic and random forces respectively, and ξ is a diagonal matrix of drag coefficients calculated using Stokes' law from the viscosity of the fluid and the dimensions of the objects. Such an equation accurately describes the motion of micrometer-sized objects in a fluid that is dominated by elastic and viscous forces. In addition to Brownian motion at each positional coordinate, the equation includes the bending elasticity of the filaments and the elastic terms associated with the molecules forming bridges between two filaments. The differential equation involving all the coordinates of all vertices is solved using a first-order semi-implicit numerical integration scheme that is numerically very stable. Moreover, at each time step, a variety of biochemical processes are modelled as first-order stochastic processes: activation, binding and unbinding, nucleation, and microtubule dynamic instability.

The cell volume is fixed and cylindrical, with a length of 11 μm and diameter of 5 μm, symmetric around the x-axis. The edges of the cell induce microtubule plus ends to stall. With this assumption, no confinement forces were needed. Microtubules thus do not track the cell edges.

Microtubule Nucleation. Microtubules are nucleated by three pathways:

N1. Kinetochores
N2. Pole-induced
N3. Augmin-mediated

Each pathway is constituted of a fixed number of nucleator entities, with properties adjusted according to the pathway that is represented: kinetochore and pole associated nucleators are anchored to beads, while the augmin-mediated nucleator is part of a diffusible complex. Each nucleator may only nucleate one microtubule at a time, and would remain inactive until this microtubule vanishes, or the nucleator detaches from it.

For pathway N1 (kinetochores), each kinetochore harbors 5 nucleators, and their nucleation rate is fixed and unregulated. Moreover, the kinetochore-based nucleator will remain attached at the plus end of the microtubules, while for the other pathways the nucleator remains attached to the minus end.

Nucleation pathway N2 (poles) consists of nucleators attached to the beads that form the condensate at the spindle pole (see below).

For nucleation pathway N3 (augmin-mediated), individual augmin entities are generated on a random position on the surface of the kinetochores with a fixed source rate. These augmin entities have a finite lifetime characterized by a constant molecular rate. This is implemented using a timer for each augmin entity, initialized with $t = -log(\theta^+)/R$, where R=5/s is the deactivation rate and θ^+ a random number in $]0,1]$. Augmin entities are deleted if their timers reach zero. During its lifetime, an augmin entity diffuses freely, and may bind to existing microtubules within its binding range, with the prescribed binding rate. A bound augmin stays fixed relative to the microtubule on which it is attached, until it unbinds. An augmin entity that is bound to a microtubule (the mother) will nucleate a new microtubule (the daughter) as determined by its nucleation rate. Unbound augmin do not nucleate. A daughter microtubule is orientated parallel to the mother microtubule, in the same direction. During the time that it is bound, the augmin entity is protected from deactivation (the internal timer is frozen). The timer restarts if the augmin detaches from the microtubules to which it is docked. These assumptions are intended to capture the control of the augmin activity by the Ran pathway,[56] where the RanGTP complex is generated at the surface of the chromatin by RCC1 and deactivated elsewhere by RanGAP, forming a sharp gradient of active Ran around the chromosomes.[57] Our assumptions capture the essential conditions that daughter microtubules are nucleated parallel to their mother microtubule,[4] in the vicinity of the chromosomes,[58] and that augmin can be transported by fluxing microtubules.[59]

We used a single scalar parameter (noted as γ) to model the fact that pathways 2 and 3 share the same molecular nucleator gamma-tubulin. When a nucleator from these two pathways is active, its nucleation rate is multiplied by $(1 - N\gamma)$, where N is the number of microtubules in the system. In this way nucleation is reduced as microtubules become more numerous until it vanishes for $N = 1/\gamma$. We used $\gamma = 0.0002$, corresponding to a maximum of 5000 microtubules, which is much above the actual number of microtubules in the simulation ($\sim$ 2000), and this limit is not reached. However, this assumption connects the nucleation activities of pathways 2 and 3, with the effect of reducing the number of pole-nucleated microtubules if the augmin activity is increased.

Microtubules are nucleated with an initial length $L_0 = 32nm$ with their plus ends in the growing state, and undergo dynamic instability at the plus ends. The minus ends are static. Dynamic instability at the plus end is implemented following a stochastic model of the GTP cap that protects microtubules from catastrophes.[60] The instantaneous microtubule growth speed is set dynamically from the total length of the microtubules at a given time point, i.e., $v_g(t) = \alpha\left(1 - \frac{1}{\Omega}\sum L_i(t)\right)$ where α is the maximum growth speed, $\sum L_i(t)$ is the total length of all microtubules at time t and the constant Ω represents the total available tubulin pool, expressed in MT length (4000 μm). These assumptions intend to represent conditions in which the amount of tubulin from which microtubules polymerize is finite. The growth speed of individual microtubules is further reduced in the presence of an antagonistic force, $f_a < 0$, by an exponential factor, e^{f_a/f_g}, where $f_g > 0$ is a characteristic "growing force" parameter.[61] This factor is always applied, but we believe that it is insignificant for the simulations presented in this work, because cell-edge induced forces were not enabled. We instead assumed that microtubules would stall upon contacting the cell edge, only growing at a fraction of their speed in the cytoplasm; specifically,

Please cite this article in press as: Romeiro Motta et al., The cell cycle controls spindle architecture in *Arabidopsis* by activating the augmin pathway, Developmental Cell (2024), https://doi.org/10.1016/j.devcel.2024.08.001

the growth speed is divided by 10. With this assumption, we recover the conditions in plant cells, where microtubules are not observed to track the edges of the cell, but instead EB1 comets vanish as they reach the cell edge. Given that the stochastic model of dynamic instability is very dependent on the rate of tubulin addition, microtubules contacting the cell edge thus rapidly undergo catastrophes in the simulation, as observed *in vivo*. Microtubules shrink at a constant shrinkage speed v_s and do not undergo rescues. Any microtubule shorter than 24 nm is deleted. After a shrinking microtubule has vanished, its nucleator is free to nucleate again.

Microtubules experience steric interactions. They repel each other via a soft-core interaction that is repulsive with a diameter $d_0 = 0nm$:

$$F(d) = k_{steric}(d - d_0), \text{if } d \leq d_0$$

where d is the distance between the two interacting filaments. This force is applied at every filament vertex that is within the steric diameter of another filament segment. It acts primarily in the direction orthogonal to the filament axis and will not prevent filaments from sliding along each other. Steric forces interfere in this way minimally with the movements induced by crosslinking motors such as kinesin-5 (Figure S1) but will induce parallel microtubules to separate their center lines $d_0 = 0nm$ apart.

Moreover, a weak force is added to bring the microtubules closer to the x-axis (parameter 'squeeze'). This force promotes the formation of the spindle poles by focusing the kinetochore fibers on the x-axis. The force magnitude is implemented as $f(u) = F_\varepsilon \tanh(u/R_z)$, with $u = \sqrt{y^2+z^2}$ and $F_\varepsilon = 0.05pN$ the maximum magnitude of the force, and $R_z = 3\mu m$ is the range at which it plateaus. The force is applied only at the minus ends, to all microtubules. This force is directed towards the x-axis, with no component parallel to the x-axis: $f(u) \times \left\{0, \frac{-y}{u}, \frac{-z}{u}\right\}$.

Kinetochores are represented by spherical particles with a radius of 180 nm. The 20 kinetochores associated with the 10 chromosomes are placed such as to form a regular metaphase plate in the middle of the cell. Ten kinetochores are placed at $x = 0.25\mu m$, while the other ten are placed at $x = -0.25\mu m$, in a mirror configuration (same y and z coordinates). The two sets of 10 kinetochores are distributed in the YZ plane such as to approximate a disc of uniform density. Specifically, 8 kinetochores are placed at the summit of a regular octagon with $y^2+z^2 = 2\mu m$, and two kinetochores are placed inside this octagon at $y = 0.6\mu m$ and $z = 0.\mu m$ and the symmetric position $\{-y, -z\}$. Each kinetochore is immobilized in translation with a Hookean link of stiffness 1000 pN/μm but is free to rotate. Thus, the metaphase alignment of the chromosomes is assumed in our model. Microtubules are allowed to grow from the kinetochores in the initialization sequence of the simulation, in the direction of the closest spindle pole (*e.g.,* toward $x > 0$ for microtubules originating from kinetochores placed at $x = 0.25\mu m$). This favors the biorientation of all kinetochores in the initial configuration. The alignment of chromosomes in the metaphase plate and the biorientation of kinetochores are two important aspects of mitotic spindle assembly that were intentionally left aside for future work, to focus on the question of how the length of the spindle is regulated by augmin.

Each kinetochore has 5 nucleating entities (ndc80) located on a cap directed towards the closest pole. Each entity may nucleate one microtubule and remains attached to its plus end until spontaneous detachment occurs, which is set at a rate of 0 s^{-1}. The nucleation rate of 1 s^{-1} implies that kinetochores have 5 microtubules attached to them most of the time. If the kinetochore unbinds (which does not occur), the associated microtubule plus end is set in a shrinking state and will thus rapidly vanish since there is no rescue. Kinetochores regulate the plus end dynamics of microtubules to which they are attached. The minus ends are not affected. A kinetochore-attached microtubule plus end grows slower than that of a regular microtubule, and its growth speed is regulated by force on the plus end f (the force in the ndc80 entity). Specifically, $v_g(t) = \left(1 - \frac{1}{\Omega}\sum L_i(t)\right)2\beta/(1+exp(-\sqrt{2}f/f_g))$, where $\beta = \alpha/$ (the amplitude of the reduction, 6, is set by the parameter 'stabilize') and where $f_g > 0$ is the microtubule's characteristic "growing force". Compared to other microtubules, the kinetochore suppresses catastrophes, reduces average growth by a factor 6, and regulates growth upon force with the factor $2/(1+exp(-\sqrt{2}f/f_g))$, which by construction is in $]0,2]$. Pulling forces will accelerate microtubule growth up to a factor 2, while pushing forces will reduce growth by a significant fraction, if the force reaches f_g.

Each spherical particle used to represent a kinetochore contains three vertices on its surface, constituting, together with the center point, a local reference frame that provides orientation in space. The ndc80 entities are placed with respect to this local reference frame, such as to form a small cluster (a 'polar cap') on one side. This cap is initially oriented towards the closest spindle pole. Kinetochores and associated microtubules are linked by Hookean links. A first type of link constrains the position of the plus end to match the position of the "ndc80" entity on the surface of the kinetochore. This link is of zero resting length and stiffness 444 pN/μm. A second type of link (parameter 'anchor_stiffness' 1 pN/μm) is used to align all the microtubules from one kinetochore, in the direction of its cap. This link is formed between the vertex of the microtubule, that is just before the plus end, and a matching virtual point built on the kinetochore reference frame, away from the kinetochore surface, at a distance equal to the separation of the microtubule vertex and its plus end. This way, a geometrically simple but realistic configuration of microtubule attachment with the kinetochore is built.

Molecular motors. Kinesin-5 and kinesin-14 are modeled as 2 linked units, forming a complex which can thus be unbound, attached to one microtubule, or attached to two microtubules. Complexes diffuse in the unbound state, can bind to one or two filaments and, when bound to two filaments, are modeled as Hookean springs with a resting length of 50 nm and various stiffness values as specified in the parameter table. Binding is determined by a rate within a binding range, and these two parameters are set following typical values for such molecules, initially measured for conventional kinesin. Subunits bind and unbind independently from each other but cannot bind to the same position on the same filament when they belong to the same complex. Diffusion of

Please cite this article in press as: Romeiro Motta et al., The cell cycle controls spindle architecture in *Arabidopsis* by activating the augmin pathway, Developmental Cell (2024), https://doi.org/10.1016/j.devcel.2024.08.001

unbound motors is not modelled explicitly; it is assumed to be sufficiently fast that a uniform spatial distribution of unbound motors is maintained. The simulation only keeps track of the number of unbound motors, but not their positions and evaluates the average number of binding events per time step using the current total length of microtubules and the cell volume. This estimate is discretized using a Poisson distribution and the corresponding number of binding events is directly implemented by picking random positions along microtubules with uniform sampling (option 'fast_diffusion').

Molecular motor units. Whereas their binding and unbinding are discrete stochastic events, bound kinesins move deterministically on microtubules at a speed which is linearly proportional to load, given by $v = v_m(1 + f_{load} \cdot d / f_{stall})$, where d is a unit vector parallel to the microtubule (in the direction preferred by the motor), f_{load} the force vector, $f_{stall} > 0$ is a characteristic stall force and v_m is the unloaded speed of the motor (positive for kinesin-5 and negative for kinesin-14). Note that with our conventions, forces that antagonize the motor preferred motion are directed opposite to d, hence a plus-end-directed motor is slowed down by forces directed towards the minus end. For a minus-end-directed motor, the unit vector d points toward the minus end. Motors detach from the microtubule side at a rate k_{off} and immediately from the microtubule ends. The detachment rates of motors are increased exponentially by the load on the motor and a characteristic unbinding force f_{unbind}, according to Kramer's law;$k = k_{off} \, exp\,(\|f_{load}\| / f_{unbind})$.

Kinesin-5 is modelled as a pair of identical motor units connected by a Hookean spring-like link with resting length d_m and stiffness K_m. This link can rotate freely at both attachment points, such that the angle between two crosslinked microtubules is unconstrained. If one motor of a pair is bound to a microtubule, the other can bind to any microtubule within a range r_b at rate k_{on}. To simulate the observed difference in kinesin-5 affinity to parallel vs. antiparallel microtubule configurations,[62] we used two separate kinesin-5 entities: an 'antikin' that may only bind antiparallel configurations and a 'parakin' that may bind to all the other configurations. The criteria defining parallel vs. antiparallel is based on the cosine of the angle formed between the direction vectors of the relevant microtubule segments (the dot product of the unit direction vector of the microtubules). The antiparallel motor may bind only if $cos(\theta) < -0.5$, and the other motor if $cos(\theta) > -0.5$. To simulate the observed differences, the 'parakin' has an unbinding rate of 0.6 s^{-1}, whereas the 'antikin' has a lower unbinding rate of 0.06 s^{-1}. The other characteristics of the two kinesin-5 subtypes are identical.

Kinesin-14 is composed of a minus-end-directed motor domain linked to a diffusible domain via a Hookean link. The minus-end-directed motors are modelled similarly to the plus-end-directed motor domains of kinesin-5, with respect to load and detachment. The non-motor domain of kinesin-14 may diffuse passively or be dragged along the side of a microtubule. It is characterized by a linear mobility coefficient μ. A domain that is under a force f transmitted through the Hookean link will move along the microtubule in the direction of the force with an average speed μf. In addition, it undergoes diffusion with a 1D diffusion constant $D_1 = \mu k_B T$, where T is the absolute temperature and k_B Boltzman's constant ($k_B T = 4.2nm.pN$). The movement in a time interval τ was implemented as $\delta = \mu f \tau + \theta\sqrt{6D_1\tau}$, where θ is a random number uniformly distributed over $[-1, 1]$. In contrast to the motor domain, the diffusible domain does not unbind immediately upon reaching the microtubule minus end. Instead, it keeps the same unbinding rate at the minus end as when located on the side of microtubules. Unbinding rates are however still modulated exponentially by the load according to Kramer's law;$k = k_{off} \, exp\,(\|f_{load}\| / f_{unbind})$. Given that it is linked to a slow minus-end-directed motor, a diffusible domain is unlikely to ever reach a growing plus end, but we have assumed anyhow that it would detach immediately at the plus end.

Spindle poles. The poles of the spindle in the simulation are made with discrete particles (hereafter referred to as beads). Initially, 1280 beads are placed at $x = 2\mu m$, and another 1280 at $x = -2\mu m$. We also tested the robustness of our simulation by changing the initial position and the number of the beads, as well as by removing kinesin-5 (Figures S1D–S1L). In most cases the simulations will converge to a steady state that is identical: the beads will form two aggregates located at the spindle poles. The only notable exception occurs if kinesin-5 is removed from the system and so no longer slides antiparallel microtubules apart, resulting in a collapsed spindle (Figure S1E).[63] We have checked placing the initial clusters at different distances from the kinetochores (Figures S1F and S1G), and displaced up or down laterally (Figures S1H and S1I). The simulation also converges to the same steady state if the beads are initially all scattered uniformly in the cell (Figure S1K), but it takes more time to reach this steady state. Accordingly, we ran simulations varying the number of pole microtubule nucleators from 0 to 2560 (Figures S2A–S2G). Our model changes smoothly over this range: a bipolar spindle is still generated without pole-nucleated MTs (Figure S2A), spindle length decreases from $\sim$ 6 μm to $\sim$ 5 μm over this range (Figure S2B), the number of pole-nucleated MTs increases from 0 to $\sim$ 350 (Figure S2D), and the mean k-fiber length decreases from $\sim$ 2 μm to $\sim$ 1.85 μm (Figure S2E). The increase in spindle length is due to longer KT-MTs, as evidenced by Figure S2E.

Two forces hold beads together and provide them with the ability to form a fluid phase within the cytoplasm: a specific pressure associated to the density of beads and a surface tension. The pressure terms ensure that the beads remain separated by a distance roughly corresponding to maximal sphere packing density. The surface tension promotes the fusion of two droplets of beads that would come into contact, in our case leading to the collapse of the spindle into a monopole. The beads behave as a fluid phase and form compact droplets at the pole which remain mostly spherical and move very little during the simulation. The density of the condensate appears uniform and close to the density value set as parameter (equal to V_{max}).

The bead fluid subsystem is modelled following the 'Smoothed Particle Hydrodynamics' (SPH) method.[64] The SPH method, which was originally developed for astrophysics, integrates well with Cytosim after adaptation to the microscopic physics in which inertia is negligible. All beads are spherical with the same radius $R = 64nm$. We assumed a uniform mass density for the beads that is equal to that of the cytoplasm, such that we simply used the volume of each particle ($m_a = 4\pi R^3/3$) and not their mass to weigh their contribution in the SPH sums. We note h the smoothing length scale ($h = 303nm$) and only used kernels with finite support, vanishing for distances d above h. The local density ρ_a is calculated using the standard 6th-order polynomial kernel $W_{poly6}(d) = W_6[h^2 - d^2]^3$,

where $W_6 = 315/64\pi h^9$ provides the normalization. With our simplification of density = 1, the mass density estimated at beads is effectively a dimensionless volume fraction. A value of pressure for each bead is then calculated as $P_a = K_{SPH}.max(0, \rho_a - V_{max})$, where V_{max} is the desired density, set to the maximum volume fraction achieved for packed spheres ($V_{max} = \pi/3\sqrt{2} \approx 0.74$), and K_{SPH} can be seen as a compressibility factor, a stiffness associated with the pressure. A pressure force is derived from the gradient of density, using Desbrun's spiky kernel $W_{spiky}(d) = W_S[h - d]^3$, where $W_S = 15/\pi h^6$,[65] using Monagan's symmetric formula (Eq. 3.3 in J. J. Monaghan. Smoothed particle hydrodynamics, 1992):

$$f_{a \leftarrow b} = -m_a m_b \left(\frac{P_a}{{\rho_a}^2} + \frac{P_b}{{\rho_b}^2}\right) \nabla W_S(r_a - r_b).$$

We used a cohesion kernel to model the surface tension,[66] with however a modified kernel:

$$W_{cohesion}(d) = W_C \begin{cases} C_K[(h-d)d]^3 - (C_K - 1)\left(\frac{h}{2}\right)^6 & if d \leq h/2 \\ [(h-d)d]^3 & if d > h/2, \end{cases}$$

where $W_C = 32/\pi h^9$ is for normalization. This kernel is continuous at $d = h/2$, and $C_K = 275/19$is adjusted to ensure that the force experienced by a particle located on the surface of a droplet of constant density would vanish, namely:

$$0 = \int_{r=0}^{h} r^2 W_{cohesion}(r) dr$$

The cohesion force is calculated using a symmetric formula:

$$f_{a \leftarrow b} = -\gamma_{SPH} m_a m_b \frac{r_a - r_b}{|r_a - r_b|} \left(\frac{2V_{max}}{\rho_a + \rho_b}\right) W_C(r_a - r_b).$$

Using a symmetric SPH formula ensures that the force will always balance, which is essential. The forces calculated per particle are then scaled by the drag coefficient of each particle (Stokes' law: $\zeta = [6\pi R]^{-1}$) to obtain their instantaneous speed, from which a displacement is calculated. We use an explicit integration if the bead is unconnected with the microtubule system ($\delta x = \zeta f \tau$). Otherwise, for instance if one of the bead's binder is attached to a microtubule, the SPH force is added to Cytosim's force engine as an explicit force term, such as to combine the SPH-calculated forces with the elastic forces associated with the links to microtubules. In any case, a random force is added to model the unbiased diffusion of beads, calibrated from their size ($D = \zeta k_B T$), the viscosity and the time-step. The full details of our SPH implementation will be given in a separate article.

Three activities are associated with the beads forming the condensate at the spindle pole: microtubule binding, nucleation and severing. The microtubule binding activity is implemented by attaching discrete binding entities to the center of the beads forming the condensate. In the spindle simulations, each bead has $\sim$ 4 binders. These binders may only bind to microtubules near their minus ends, specifically at a location of the microtubule that is less than 1 μm away from the minus end, provided the distance to the bead center (where the binder is anchored) is lower than 80 nm. The nucleation activity is implemented by attaching one nucleator per bead (see above for the detailed description of the nucleation model). The microtubule severing activity is implemented similarly to the augmin complex: "cutters" with two katanin units are generated at the surface of the beads with a 'source' rate and destroyed stochastically with a constant rate of 8 s^{-1}. These entities are free to diffuse and to bind to microtubules during their lifetime. In this way a permanent gradient of severing activity is generated within and around the condensate. In addition, 64 entities containing one single katanin are set freely diffusing in the entire simulation volume. Each severing unit can cut a microtubule to which it is bound with a rate of 0.2 s^{-1}. Upon cutting the severing unit unbinds. The new plus end is created in the shrinking state, as widely observed.[67] The new minus end is static.

TEM of Arabidopsis root cross-sections

Roots were fixed with 2% glutaraldehyde in cacodylate buffer (75 mM, pH 7.0) for 3.5 h, postfixed with 1% osmium tetroxide at 4°C overnight. Samples were dehydrated through a series of graded acetone concentrations, 30% to 100%, and finally embedded in plastic according to Spurr.[68] Ultrathin sections were obtained with an ultramicrotome (Ultracut E, Leica-Reichert-Jung, Nußloch, Germany) and stained with uranyl acetate followed by lead citrate.[69] Sections were viewed with a LEO 906 E TEM (LEO, Oberkochen, Germany) equipped with the Wide-angle-2K (4Mpx.) Dual Speed CCD Camera (TRS, Moorenweis, Germany) using the software ImageSP-Professional to acquire, visualize, analyse, and process image data.

AP-MS on CYCB3;1

Cloning of CYCB3;1 encoding the C-terminal GS^{rhino} tag[70] fusion under control of the constitutive cauliflower tobacco mosaic virus 35S promoter and transformation of Arabidopsis cell suspension cultures (PSB-D) with direct selection in liquid medium was carried out as previously described.[71]

Pull downs were performed in triplicate, using in-house prepared magnetic IgG beads and 25 mg of total protein extract per pull down as described.[71] On-bead digested samples were analyzed on a Q Exactive (ThermoFisher Scientific) and co-purified proteins were identified with Mascot (Matrix Science) using standard procedures.[71]

Please cite this article in press as: Romeiro Motta et al., The cell cycle controls spindle architecture in *Arabidopsis* by activating the augmin pathway, Developmental Cell (2024), https://doi.org/10.1016/j.devcel.2024.08.001

After identification, the protein list was filtered versus a large dataset of similar experiments with non-related baits using calculated average Normalized Spectral Abundance Factors (NSAFs).[71] Proteins identified with at least two matched high confident peptides in at least two experiments, showing high (at least 10-fold) AND significant [$-\log_{10}(p\text{-value(T-test)}) \geq 10$] enrichment compared to the large dataset were retained.

Root growth assays and timing of mitotic divisions on oryzalin

For the oryzalin root growth assays, seeds were sown on ½ MS with either 0.05% DMSO as a control or oryzalin. To follow mitotic cell divisions on control or oryzalin conditions live, whole five- to seven-day-old seedlings were placed in a glass-bottom dish and covered in solid ½ MS followed by the addition of liquid ½ MS containing 0.05% DMSO as a control or 150 nM oryzalin and incubation for 1 hour. Oryzalin stocks were prepared in DMSO at a concentration of 100 mM and stored at -20°C.

Wholemount immunolocalization of α-tubulin and KNOLLE in roots

Roots of 4-day-old Arabidopsis seedlings were fixed in 4% paraformaldehyde and 0.1% Triton X-100 in MTSB 1/2 buffer (25 mM PIPES, 2.5 mM MgSO4, 2.5 mM EGTA, pH 6.9) for 1 hour under vacuum, then rinsed in PBS 1X for 10 minutes. Samples were then permeabilized in ethanol for 10 minutes and rehydrated in PBS for 10 minutes. Cell walls were digested using the following buffer for one hour: 2 mM MES pH 5, 0.20% driselase and 0.15% macerozyme. Tissues were hybridized overnight at room temperature with the B-5-1-2 monoclonal anti-α-tubulin (Sigma) and the anti-KNOLLE antibody[49] (kind gift of G. Jürgens, University of Tübingen, Germany). The next day, tissues were washed for 15 minutes in PBS, 50 mM glycine, incubated with secondary antibodies (Alexa Fluor 555 goat anti-rabbit for KNOLLE antibody and Alexa Fluor 488 goat anti-mouse for the tubulin antibody) overnight and washed again in PBS, 50 mM glycine and DAPI 20 ng/ml. Tissues were mounted in VECTASHIED and DAPI and viewed using an SP8 confocal laser microscope (Leica Microsystems).

Samples were excited sequentially at 405 nm (DAPI), 488 nm (@TUB/Alexa Fluor 488), and 561 nm (@KNOLLE/Alexa Fluor 555), with an emission band of 420-450 nm (DAPI), 495-545 nm (Alexa Fluor 488), and 560-610 nm (Alexa Fluor 555) using a PMT for DAPI imaging, and hybrid detectors for MT and KNOLLE imaging. All stacks were imaged using the same zoom (x 1,60) with a voxel size xyz of 200 nm x 200 nm x 500 nm.

Immunolocalization of α- and γ-tubulin in root meristematic cells

Root cells were immunostained as described in Liu et al.[72] α-tubulin was stained using a monoclonal antibody raised in mouse (Sigma, T9026) and γ-tubulin was stained using a monoclonal antibody also raised in mouse (Agrisera, AS20 4482). Since the primary antibodies were raised in the same species, a sequential staining method was employed. First, the slides were incubated with the γ-tubulin antibody overnight at 4°C followed by incubation with the secondary antibody against mouse STAR 635P (abberior) at room temperature for 2 hours. Next, the slides were incubated with the α-tubulin antibody overnight at 4°C followed by incubation with the secondary antibody against mouse STAR 580 (abberior) at room temperature for 2 hours. Samples were then mounted in VECTASHIELD containing DAPI (Vector Laboratories). Slides were imaged in a Zeiss LSM 880 microscope equipped with Airyscan and images were acquired with a voxel size of 49 nm x 49 nm x 160 nm.

Protein expression and purification and *in vitro* kinase assay

To generate HisGST-EDE1, the *CDS* of EDE1 was initially amplified by PCR with primers containing attB1/attB2 flanking sequences followed by a Gateway BP reaction into pDONR221 and subsequently a Gateway LR reaction into the pHGGWA vector. The destination vector was then transformed in *E. coli* BL21 (DE3) pLysS cells. For expression, *E. coli* cultures were grown until an OD of 0.6 followed by addition of IPTG at a concentration of 0.2 mM and incubation at 16°C overnight. The CDKB1;1-CYCB3;1 complex was expressed and purified as described previously.[50] After purification with Ni-NTA agarose or Strep-Tactin in case of the CDKB1;1 control, all proteins were desalted using PD MiniTrap G-25 columns (GE Healthcare) and protein quality was checked by CBB staining and immunoblotting. Kinase assays were incubated at 30°C for 1 hour in a buffer containing 50 mM Tris-HCl, pH 7.5, 10 mM $MgCl_2$, 0.5 mM ATP and 5 mM DTT.

Sample preparation and LC-MS/MS data acquisition for the identification of EDE1 phosphosites

The protein mixtures were reduced with dithiothreitol, alkylated with chloroacetamide, and digested with trypsin. These digested samples were desalted using StageTips with C18 Empore disk membranes (3 M),[73] dried in a vacuum evaporator, and dissolved in 2% ACN, 0.1% TFA. Samples were analyzed using an EASY-nLC 1200 (Thermo Fisher) coupled to a Q Exactive Plus mass spectrometer (Thermo Fisher).

For initial assessment of phosphosites, peptides (1:10 dilution) were separated on 16 cm frit-less silica emitters (New Objective, 75 μm inner diameter), packed in-house with reversed-phase ReproSil-Pur C18 AQ 1.9 μm resin (Dr. Maisch). Peptides were loaded on the column and eluted for 50 min using a segmented linear gradient of 5% to 95% solvent B (0 min: 5%B; 0-5 min -> 5%B; 5-25 min -> 20%B; 25-35 min ->35%B; 35-40 min -> 95%B; 40-50 min ->95%B) (solvent A 0% ACN, 0.1% FA; solvent B 80% ACN, 0.1%FA) at a flow rate of 300 nL/min. Mass spectra were acquired in data-dependent acquisition mode with a TOP15 method. MS spectra were acquired in the Orbitrap analyzer with a mass range of 300–1500 m/z at a resolution of 70,000 FWHM and a target value of 3×10^6 ions. Precursors were selected with an isolation window of 1.3 m/z. HCD fragmentation was performed at a normalized collision energy of 25. MS/MS spectra were acquired with a target value of $5\text{x}10^5$ ions at a resolution of 17,500 FWHM,

a maximum injection time of 120 ms and a fixed first mass of m/z 100. Peptides with a charge of 1, greater than 6, or with unassigned charge state were excluded from fragmentation for MS^2; dynamic exclusion for 20s prevented repeated selection of precursors.

For the targeted analysis, samples (1:3 dilution) were resolved using the above-mentioned segmented linear gradient. The acquisition method consisted of a full scan method combined with a non-scheduled PRM method. The 17 targeted precursor ions were selected based on the results of DDA peptide search in Skyline. MS spectra were acquired in the Orbitrap analyzer with a mass range of 300–2000 m/z at a resolution of 70,000 FWHM and a target value of 3×10^6 ions, followed by MS/MS acquisition for the 17 targeted precursors. Precursors were selected with an isolation window of 2.0 m/z. HCD fragmentation was performed at a normalized collision energy of 27. MS/MS spectra were acquired with a target value of $2x10^5$ ions at a resolution of 17,500 FWHM, a maximum injection time of 120 ms and a fixed first mass of m/z 100.

MS data analysis and PRM method development

Raw data from DDA acquisition were processed using MaxQuant software (version 1.5.7.4, http://www.maxquant.org/).[52] MS/MS spectra were searched by the Andromeda search engine against a database containing the respective proteins used for the *in vitro* reaction. Trypsin specificity was required and a maximum of two missed cleavages allowed. Minimal peptide length was set to seven amino acids. Carbamidomethylation of cysteine residues was set as fixed, phosphorylation of serine, threonine and tyrosine, oxidation of methionine and protein N-terminal acetylation as variable modifications. The match between runs option was disabled. Peptide-spectrum-matches and proteins were retained if they were below a false discovery rate of 1% in both cases.

Raw data from the DDA acquisition were analyzed on MS1 level using Skyline (https://skyline.ms)[53] and a database containing the respective proteins used for the *in vitro* reaction. Trypsin specificity was required and a maximum of two missed cleavages allowed. Minimal peptide length was set to seven maximum length to 25 amino acids. Carbamidomethylation of cysteine, phosphorylation of serine, threonine and tyrosine, oxidation of methionine and protein N-terminal acetylation were set as modifications. Results were filtered for precursor charges of 2, 3 and 4. For each phosphorylated precursor ion a respective non-phosphorylated precursor ion was targeted as a control, furthermore several precursor ions from the backbone of EDE1 were chosen as controls between the samples. In total 17 precursors were chosen to be targeted with a PRM approach.

After acquisition of PRM data the raw data were again processed using MaxQuant software, with above-mentioned parameters. Table S6 shows phosphosites and localization probabilities obtained using the MaxQuant search. The mass spectrometry proteomics data have been deposited to the ProteomeXchange Consortium via the PRIDE[74] partner repository with the dataset identifier PXD046697.

Generation of the GFP-EDE1 reporter

To create the PRO_{EDE1}*:EGFP:EDE1* construct, the genomic fragment of *EDE1* was amplified by PCR and cloned into *pDONR221*. A SmaI site was inserted at the N-terminus of *EDE1* before the first *ATG* codon. The *EDE1* construct containing the SmaI restriction site was linearized by SmaI digestion and ligated to the *EGFP* gene, followed by an LR recombination reaction with the destination vector *pGWB501*. Primers used in this study are listed in Table S7.

FRAP assay

For the bleaching of GFP-EDE1, sections of the spindles were bleached with the 405 and 488 lasers both at 100% after 5 frames of imaging and with a scan speed of 7 and 5 iterations. Images were acquired every 0.5 s with a pixel size of 120 nm. For the bleaching of TagRFP-TUA5 in the GFP-EDE1/*ede1-1* and GFP-$EDE1^{8A}$/*ede1-1* backgrounds, spindles were bleached with the 405 laser only at 100% and a scan speed of 5 and 10 iterations with a pixel size of 100 nm.

QUANTIFICATION AND STATISTICAL ANALYSIS

Experimental determination of spindle parameters

For the estimation of the number of spindle microtubules, we analyzed TEM images of cross-sections of roots. We measured the number of microtubules in a 1 μm^2 square. Next, we extrapolated this value to an area of approximately 16 μm^2 for one half of the spindle. With this, we reached a value that varied between 576 and 1,408 microtubules for a full root spindle (n = 5).

For estimating the number of microtubules in kinetochore fibers, we counted the number of microtubules in bundles from TEM images and measured the fluorescence intensity of kinetochore fibers from spindles stained against α-tubulin compared to single microtubules in the same cell. For the fluorescence measurements, we drew a line across a single microtubule in Fiji and measured the integrated density divided by the area analyzed. Next, we measured the integrated density divided by the area analyzed in kinetochore fibers and divided that by the value obtained for a single microtubule to obtain an estimate of number of microtubules. This fluorescence intensity estimate was obtained from four different cells. We obtained similar values in both experimental approaches.

For determining the growth speed of microtubules, we generated kymographs using the KymographBuilder Fiji plugin (https://imagej.net/plugins/kymograph-builder) from roots of plants expressing an $EB1b_{PRO}$*::EB1b-GFP* reporter that were imaged with a spinning disk microscope with a 0.5 s frame rate. Values were obtained for ten microtubules per spindle from three spindles, each from an independent plant.

Please cite this article in press as: Romeiro Motta et al., The cell cycle controls spindle architecture in *Arabidopsis* by activating the augmin pathway, Developmental Cell (2024), https://doi.org/10.1016/j.devcel.2024.08.001

Spindle morphogenesis image analysis

First, an ellipse was fitted manually in Fiji[51] to spindles tagged with TagRFP-TUA5 or immunostained against α-tubulin. Next, the major axis, minor axis and spindle area measurements were obtained by going to Analyze > Set measurements and checking the "Area" and "Fit ellipse" boxes. All values are provided in Table S2. To judge the presence of visible astral microtubules in individual spindle images, spindle files were anonymized in Fiji with the Blind Analysis Tools plugin (https://imagej.net/plugins/blind-analysis-tools). To analyse γ-tubulin distribution, the images (with a 49 nm pixel size) were first equally treated with the Gaussian Blur filter with a radius of 0.05 scaled units to improve the fluorescence intensity peak definition. Then, a line was drawn exactly at the middle of the spindle through the pole-to-pole axis in a perpendicular angle in relation to the spindle midzone and the fluorescence intensity profile was plotted in Fiji. The fluorescence intensity values were then normalized by the minimum and maximum values in each cell and combined into a graph containing the mean and SD values of each replicate. The distance between the two highest values of fluorescence was calculated individually in every cell and then corrected by the spindle major axis and plotted as a ratio. In the case of the analysis of GFP-EDE1 distribution, the images (with a 143 nm pixel size) were treated with Gaussian Blur with a radius of 0.1 scaled units.

Root growth assays on oryzalin

Root growth was recorded daily up until 5 days after germination when plates were scanned and subsequently manually analyzed with Fiji.

Wholemount immunolocalization of α-tubulin and KNOLLE in roots

A blind counting was set up to count mitotic microtubule arrays. Six roots per genotype were analyzed for WT, *cycb3* and *cdkb1*, and seven roots were analyzed for *ede1-1* transformed with GFP-EDE1 WT, GFP-EDE1^{8A} and GFP-EDE1^{8D}. All images were first anonymized, and mitotic microtubule arrays were counted within each root stack using the "Cell counter" ImageJ plugin (https://imagej.nih.gov/ij/plugins/cell-counter.html).

FRAP assay

For the analysis of bleached regions, the Stowers Plugins Collection was used (https://research.stowers.org/imagejplugins). The data processing and analysis was performed as previously described.[75] Outliers in the half maximum values were removed using the ROUT method (Q = 5%).

Statistical software

All statistics tests were performed with GraphPad Prism. All graphs (with the exception of Figures 7, S2B–S2G, and S6) were plotted in GraphPad Prism.